Chapter 1

Choice of regularization and numerical results

This chapter addresses the problem of choosing appropriate regularization and preconditioning operators. Such a choice plays a crucially important role in iterative data regularization. I discuss three strategies appropriate for different kinds of data:

1. Smoothly varying surfaces are regularized with recursive helical smoothers based on the tension-spline theory.
2. The local plane-wave model is often suitable for characterizing different kinds of seismic data. Such data are successfully regularized with plane-wave destructor filters.
3. Seismic reflection data exhibit additional degrees of predictability because of multiple coverage. They can be regularized with finite-difference offset continuation filters. Among the three methods being discussed, the offset continuation approach is the most innovative. The theory behind it is explained in Chapter 6.

Combining the constructed regularization operator **D** with the appropriate forward operator **L**, discussed in Chapter **??**, we obtain a complete problem formulation in the form of system (**??**) or (**??**). This chapter is the culmination of this dissertation. It contains final numerical experiments that test and illustrate the main concepts developed in other chapters.

REGULARIZING SMOOTH DATA WITH SPLINES IN TENSION

The method of minimum curvature is an old and ever-popular approach for constructing smooth surfaces from irregularly spaced data (Briggs, 1974). The surface of minimum curvature corresponds to the minimum of the Laplacian power or, in an alternative formulation, satisfies the biharmonic differential equation. Physically, it models the behavior of an elastic plate. In the one-dimensional case, the minimum curvature method leads to the natural cubic spline interpolation (de Boor, 1978). In the two-dimensional case, a surface can be interpolated with biharmonic splines (Sandwell, 1987) or gridded with an iterative finite-difference scheme (Swain, 1976). According to the general optimization method, outlined in Chapter **??**, I approach the gridding (data regularization) problem with an iterative least-squares optimization scheme.

In most of the practical cases, the minimum-curvature method produces a visually pleasing smooth surface. However, in cases of large changes in the surface gradient, the method can create strong artificial oscillations in the unconstrained regions. Switching to lower-order methods, such as minimizing the power of the gradient, solves the problem of extraneous inflections, but also removes the smoothness constraint and leads to gradient discontinuities (Fomel and Claerbout, 1995). A remedy, suggested by Schweikert (1966), is known as *splines in tension*. Splines in tension are constructed by minimizing a modified quadratic form that includes a tension term. Physically, the additional term corresponds to tension in elastic plates (Timoshenko and Woinowsky-Krieger, 1968). Smith and Wessel (1990) developed a practical algorithm of 2-D gridding with splines in tension and implemented it in the popular GMT software package.

In this section, I develop an application of helical preconditioning to gridding with splines in tension. Following the results of Chapter **??**, I accelerate an iterative data regularization algorithm by recursive preconditioning with multidimensional filters defined on a helix (Claerbout, 1998a). The efficient Wilson-Burg spectral factorization constructs a minimum-phase filter suitable for recursive filtering.

I introduce a family of 2-D minimum-phase filters for different degrees of tension. The filters are constructed by spectral factorization of the corresponding finite-difference forms. In

the case of zero tension (the original minimum-curvature formulation), we obtain a minimum-phase version of the Laplacian filter. The case of infinite tension leads to spectral factorization of the Laplacian and produces the known *helical derivative* filter (Claerbout, 1999; Zhao, 1999).

The tension filters can be applied not only for data regularization but also for preconditioning in any estimation problems with smooth models. Tomographic velocity estimation is an obvious example of such an application (Woodward et al., 1998).

Mathematical theory of splines in tension

The traditional minimum-curvature criterion implies seeking a two-dimensional surface $f(x,y)$ in region D, which corresponds to the minimum of the Laplacian power:

$$\iint\limits_D \left|\nabla^2 f(x,y)\right|^2 dx\,dy\,, \tag{1.1}$$

where ∇^2 denotes the Laplacian operator: $\nabla^2 = \frac{\partial^2}{\partial x^2} + \frac{\partial^2}{\partial y^2}$.

Alternatively, we can seek $f(x,y)$ as the solution of the biharmonic differential equation

$$(\nabla^2)^2 f(x,y) = 0\,. \tag{1.2}$$

Equation (1.2) corresponds to the normal system of equations in the least-square optimization problem (**??**), the Laplacian operator being **D**, and the surface $f(x,y)$ corresponding to the unknown model **m**. Fung (1965) and Briggs (1974) derive equation (1.2) directly from (1.1) with the help of the variational calculus and Gauss's theorem.

Formula (1.1) approximates the strain energy of a thin elastic plate (Timoshenko and Woinowsky-Krieger, 1968). Taking tension into account modifies both the energy formula (1.1) and the corresponding equation (1.2). Smith and Wessel (1990) suggest the following form of the modified equation:

$$\left[(1-\lambda)(\nabla^2)^2 - \lambda(\nabla^2)\right] f(x,y) = 0\,, \tag{1.3}$$

where the tension parameter λ ranges from 0 to 1. The corresponding energy functional is

$$\iint_D \left[(1-\lambda) \left| \nabla^2 f(x,y) \right|^2 + \lambda \left| \nabla f(x,y) \right|^2 \right] dx\, dy \,. \tag{1.4}$$

Zero tension leads to the biharmonic equation (1.2) and corresponds to the minimum curvature construction. The case of $\lambda = 1$ corresponds to infinite tension. Although infinite tension is physically impossible, the resulting Laplace equation does have the physical interpretation of a steady-state temperature distribution. An important property of harmonic functions (solutions of the Laplace equation) is that they cannot have local minima and maxima in the free regions. With respect to interpolation, this means that, in the case of $\lambda = 1$, the interpolation surface will be constrained to have its local extrema only at the input data locations.

Norman Sleep (2000, personal communication) points out that if the tension term $\lambda\nabla^2$ is written in the form $\nabla \cdot (\lambda \nabla)$, we can follow an analogy with heat flow and electrostatics and generalize the tension parameter λ to a local function depending on x and y. In a more general form, λ could be a tensor allowing for an anisotropic smoothing in some predefined directions similarly to Clapp's steering-filter method (Clapp et al., 1997).

To interpolate an irregular set of data values, f_k at points (x_k, y_k), we need to solve equation (1.3) under the constraint

$$f(x_k, y_k) = f_k \,, \tag{1.5}$$

which translates to equation (**??**) in the linear operator notation. Using the results of Chapter **??**, we can accelerate the solution by recursive filter preconditioning. If **A** is the discrete filter representation of the differential operator in equation (1.3), and we can find a minimum-phase filter **D** whose autocorrelation is equal to **A**, then an appropriate preconditioning operator is a recursive inverse filtering with the filter **D**. Formulating the problem in helical coordinates (Claerbout, 1998a,b) enables both the spectral factorization of **A** and the inverse filtering with **D**.

Finite differences and spectral factorization

In the one-dimensional case, one finite-difference representation of the squared Laplacian is as a centered 5-point filter with coefficients $(1, -4, 6, -4, 1)$. On the same grid, the Laplacian operator can be approximated to the same order of accuracy with the filter $(1/12, -4/3, 5/2, -4/3, 1/12)$. Combining the two filters in accordance with equation (1.3) and performing a spectral factorization with one of the standard methods (Claerbout, 1976, 1992), we can obtain a 3-point minimum-phase filter suitable for inverse filtering. Figure 1.1 shows a family of one-dimensional minimum-phase filters for different values of the parameter λ. Figure 1.2 demonstrates the interpolation results obtained with these filters on a simple one-dimensional synthetic. As expected, a small tension value ($\lambda = 0.01$) produces a smooth interpolation, but creates artificial oscillations in the unconstrained regions around sharp changes in the gradient. The value of $\lambda = 1$ leads to linear interpolation with no extraneous inflections but with discontinuous derivatives. Intermediate values of λ allow us to achieve a compromise: a smooth surface with constrained oscillations.

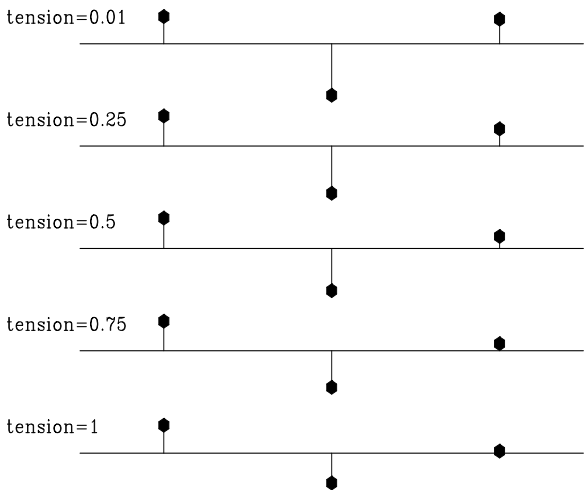

Figure 1.1: One-dimensional minimum-phase filters for different values of the tension parameter λ. The filters range from the second derivative for $\lambda = 0$ to the first derivative for $\lambda = 1$. regul-otens [ER]

To design the corresponding filters in two dimensions, I define the finite-difference representation of operator (1.3) on a 5-by-5 stencil. The filter coefficients are chosen with the help of the Taylor expansion to match the desired spectrum of the operator around the zero spatial frequency. The matching conditions lead to the following set of coefficients for the squared Laplacian:

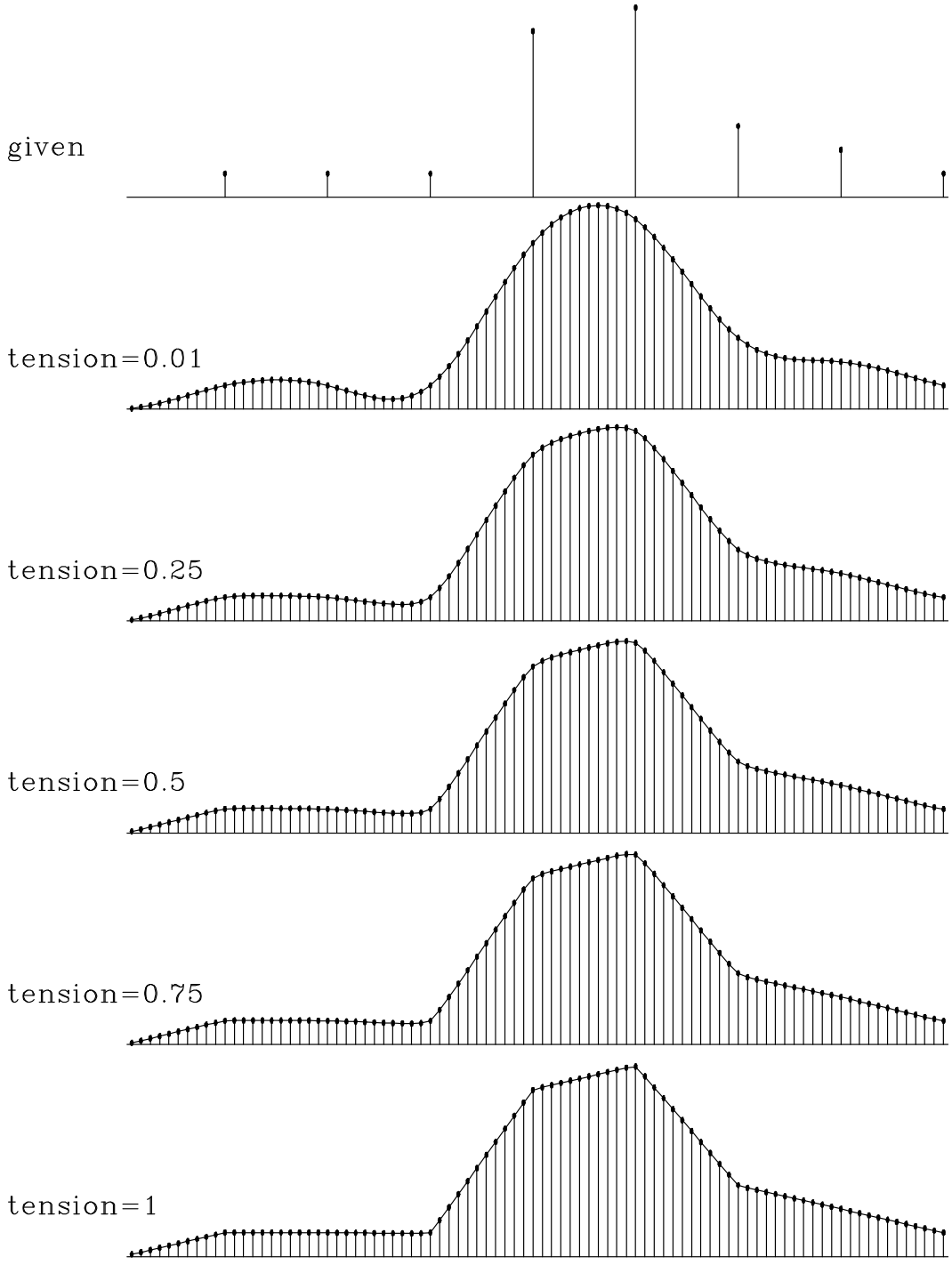

Figure 1.2: Interpolating a simple one-dimensional synthetic with recursive filter preconditioning for different values of the tension parameter λ. The input data are shown on the top. The interpolation results range from a natural cubic spline interpolation for $\lambda = 0$ to linear interpolation for $\lambda = 1$. regul-int [ER,M]

-1/60	2/5	7/30	2/5	-1/60
2/5	-14/15	-44/15	-14/15	2/5
7/30	-44/15	57/5	-44/15	7/30
2/5	-14/15	-44/15	-14/15	2/5
-1/60	2/5	7/30	2/5	-1/60

$= 1/60$

-1	24	14	24	-1
24	-56	-176	-56	24
14	-176	684	-176	14
24	-56	-176	-56	24
-1	24	14	24	-1

The Laplacian representation with the same order of accuracy has the coefficients

-1/360	2/45	0	2/45	-1/360
2/45	-14/45	-4/5	-14/45	2/45
0	-4/5	41/10	-4/5	0
2/45	-14/45	-4/5	-14/45	2/45
-1/360	2/45	0	2/45	-1/360

$= 1/360$

-1	16	0	16	-1
16	-112	-288	-112	16
0	-288	1476	-288	0
16	-112	-288	-112	16
-1	16	0	16	-1

For the sake of simplicity, I assumed equal spacing in the x and y direction. The coefficients can be easily adjusted for anisotropic spacing. Figures 1.3 and 1.4 show the spectra of the finite-difference representations of operator (1.3) for the different values of the tension parameter. The finite-difference spectra appear to be fairly isotropic (independent on angle in polar coordinates). They match the exact expressions at small frequencies.

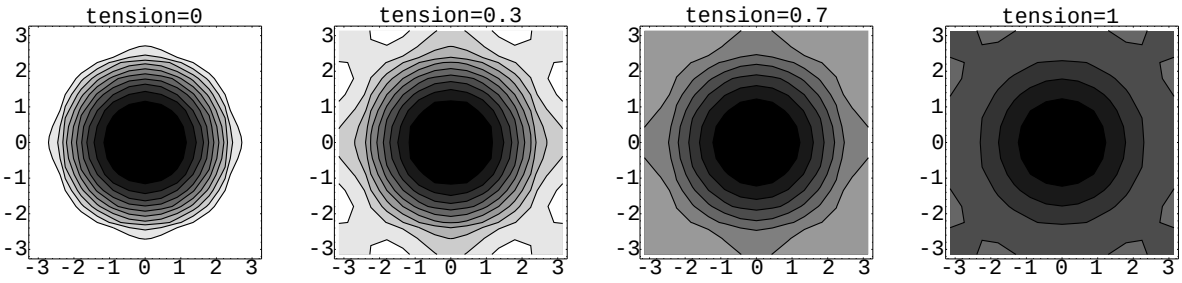

Figure 1.3: Spectra of the finite-difference splines-in-tension schemes for different values of the tension parameter (contour plots). regul-specc [CR]

Regarding the finite-difference operators as two-dimensional auto-correlations and applying the efficient Wilson-Burg method of spectral factorization described in Chapter **??**, I obtain two-dimensional minimum-phase filters suitable for inverse filtering. The exact filters contain

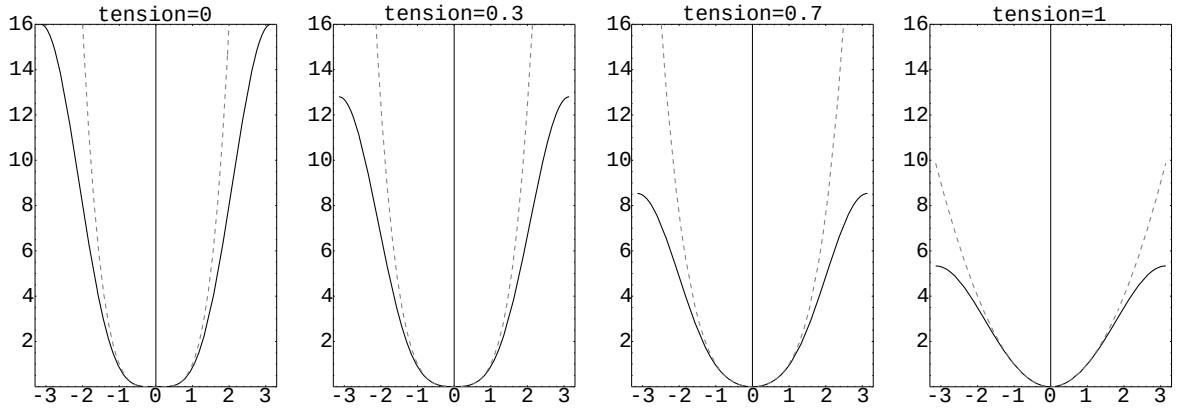

Figure 1.4: Spectra of the finite-difference splines-in-tension schemes for different values of the tension parameter (cross-section plots). The dashed lines show the exact spectra for continuous operators. regul-specp [CR]

many coefficients, which rapidly decrease in magnitude at a distance from the first coefficient. For reasons of efficiency, it is advisable to restrict the shape of the filter so that it contains only the significant coefficients. Keeping all the coefficients that are 1000 times smaller in magnitude than the leading coefficient creates a 53-point filter for $\lambda = 0$ and a 35-point filter for $\lambda = 1$, with intermediate filter lengths for intermediate values of λ. Keeping only the coefficients that are 200 times smaller that the leading coefficient, we obtain 25- and 16-point filters for respectively $\lambda = 0$ and $\lambda = 1$. The restricted filters do not factor the autocorrelation exactly but provide an effective approximation of the exact factors. As outputs of the Wilson-Burg spectral factorization process, they obey the minimum-phase condition.

Figure 1.5 shows the two-dimensional filters for different values of λ and illustrates inverse recursive filtering, which is the essence of the helix method (Claerbout, 1998a,b, 1999). The case of $\lambda = 1$ leads to the filter known as *helix derivative* (Claerbout, 1999; Zhao, 1999). The filter values are spread mostly in two columns. The other boundary case ($\lambda = 0$) leads to a three-column filter, which serves as the minimum-phase version of the Laplacian. This filter has been shown previously in Figure **??**. As expected from the theory, the inverse impulse response of this filter is noticeably smoother and wider than the inverse response of the helix derivative. Filters corresponding to intermediate values of λ exhibit intermediate properties.

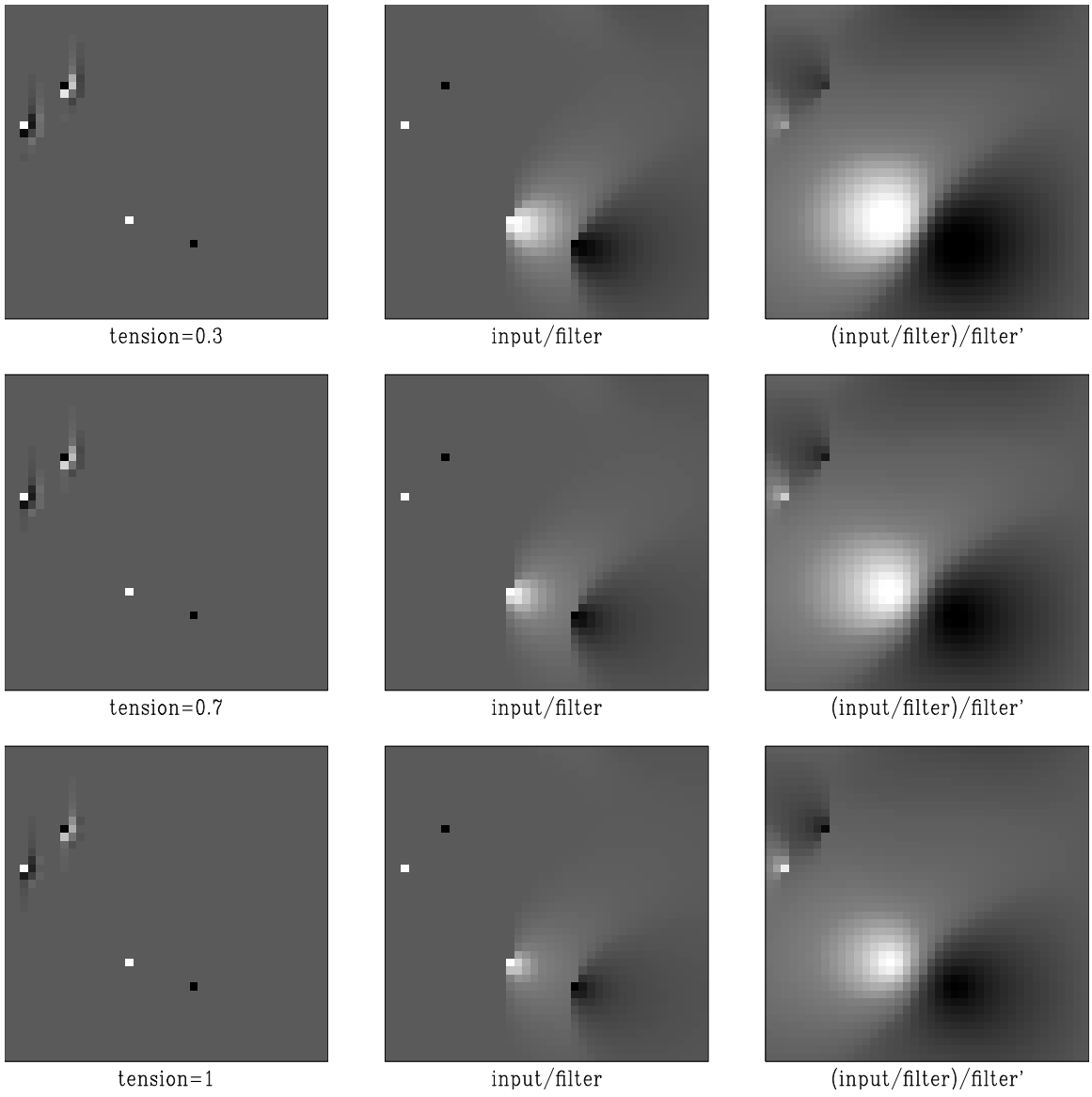

Figure 1.5: Inverse filtering with the tension filters. The left plots show the inputs composed of filters and spikes. Inverse filtering turns filters into impulses and turns spikes into inverse filter responses (middle plots). Adjoint filtering creates smooth isotropic shapes (right plots). The tension parameter takes on the values 0.3, 0.7, and 1 (from top to bottom). The case of zero tension corresponds to Figure **??**. regul-splin [ER,M]

Theoretically, the inverse impulse response of the filter corresponds to the Green's function of equation (1.3). The theoretical Green's function for the case of $\lambda = 1$ is

$$G = \frac{1}{2\pi} \ln r \ , \tag{1.6}$$

where r is the distance from the impulse: $r = \sqrt{(x - x_k)^2 + (y - y_k)}$. In the case of $\lambda = 0$, the Green function is smoother at the origin:

$$G = \frac{1}{8\pi} r^2 \ln r \ . \tag{1.7}$$

The theoretical Green's function expression for an arbitrary value of λ is unknown, but we can assume that its smoothness lies between the two boundary conditions.

In the next subsection, I illustrate an application of helical inverse filtering to a two-dimensional interpolation problem.

Regularization example

I chose an environmental Galilee dataset (Fomel and Claerbout, 1995; Claerbout, 1999) for a simple illustration of smooth data regularization. The data were collected on a bottom sounding survey of the Sea of Galilee in Israel (Ben-Avraham et al., 1990). The data contain a number of noisy, erroneous and inconsistent measurements, which present a challenge for the traditional estimation methods.

Figure 1.6 shows the data after a nearest-neighbor binning to a regular grid. The data were then passed to an interpolation program to fill the empty bins. The results (for different values of λ) are shown in Figures 1.7 and 1.8. Interpolation with the minimum-phase Laplacian ($\lambda = 0$) creates a relatively smooth interpolation surface but plants artificial "hills" around the edge of the sea. This effect is caused by large gradient changes and is similar to the sidelobe effect in the one-dimensional example (Figure 1.2). It is clearly seen in the cross-section plots in Figure 1.8. The abrupt gradient change is a typical case of a shelf break. It is caused by a combination of sedimentation and active rifting. Interpolation with the helix derivative ($\lambda = 1$)

is free from the sidelobe artifacts, but it also produces an undesirable non-smooth behavior in the middle part of the image. As in the one-dimensional example, intermediate tension allows us to achieve a compromise: smooth interpolation in the middle and constrained behavior at the sides of the sea bottom.

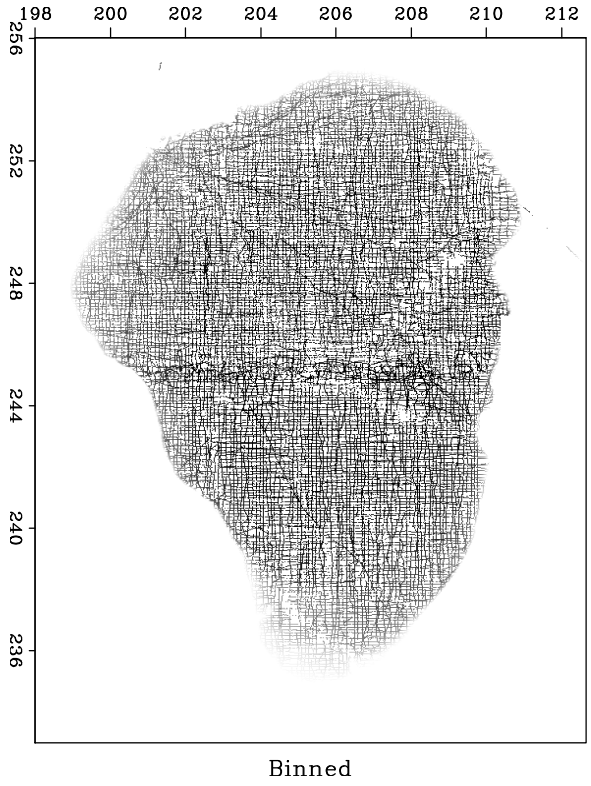

Figure 1.6: The Sea of Galilee dataset after a nearest-neighbor binning. The binned data is used as an input for the missing data interpolation program. regul-mesh [ER]

Smooth surfaces are rarely encountered in the practice of seismic exploration. In the next section, I develop a regularization operator suitable for characterizing more typical models of seismic data.

REGULARIZING LOCAL PLANE WAVES WITH PLANE-WAVE DESTRUCTOR FILTERS

Plane-wave destructor filters, introduced by Claerbout (1992), serve the purpose of characterizing seismic images by a superposition of local plane waves. They are constructed as finite-difference stencils for the plane-wave differential equation. In many cases, a local plane-wave

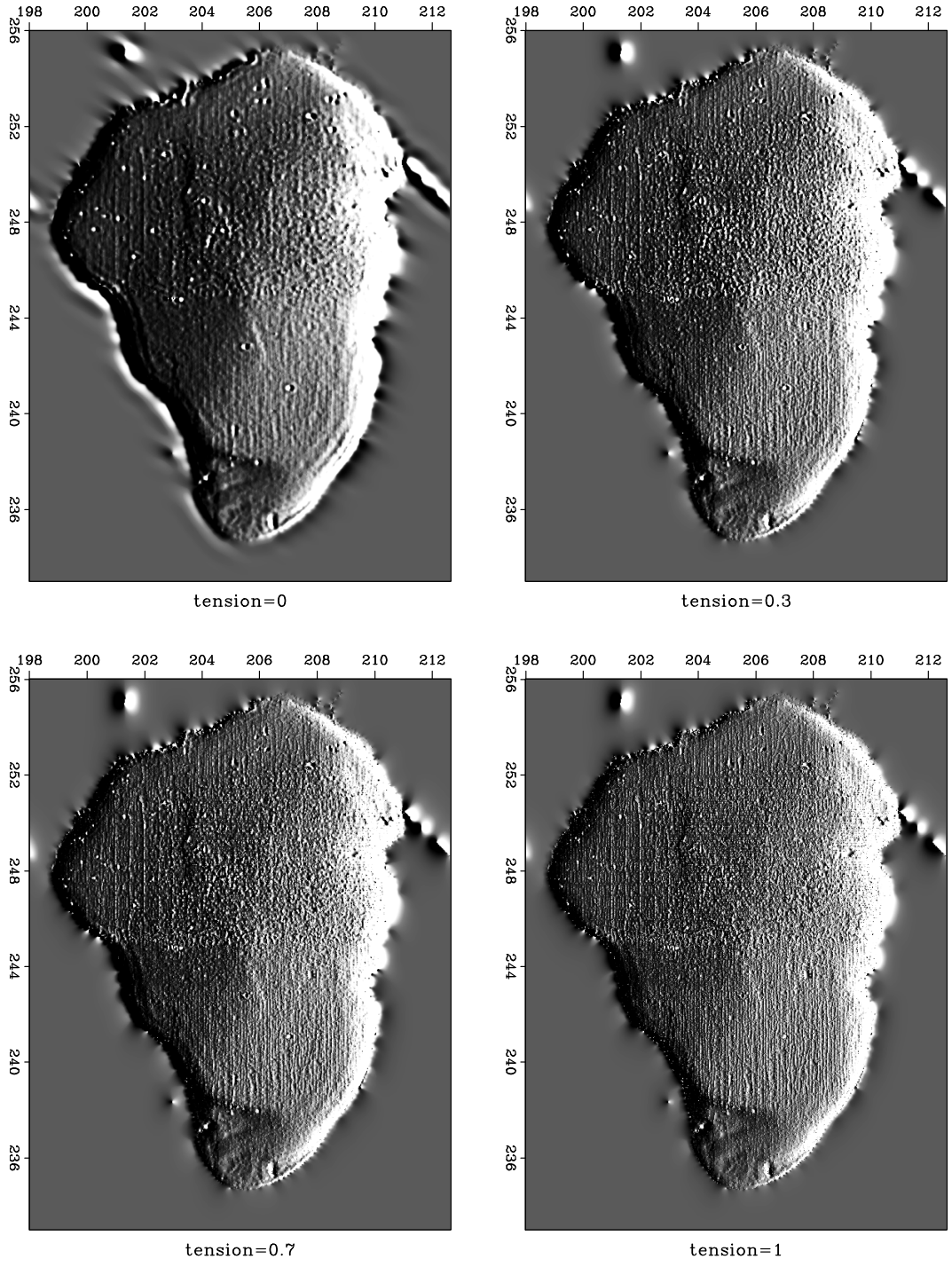

Figure 1.7: The Sea of Galilee dataset after missing data interpolation with helical preconditioning. Different plots correspond to different values of the tension parameter. An east-west derivative filter was applied to illuminate the surface. regul-gal [ER,M]

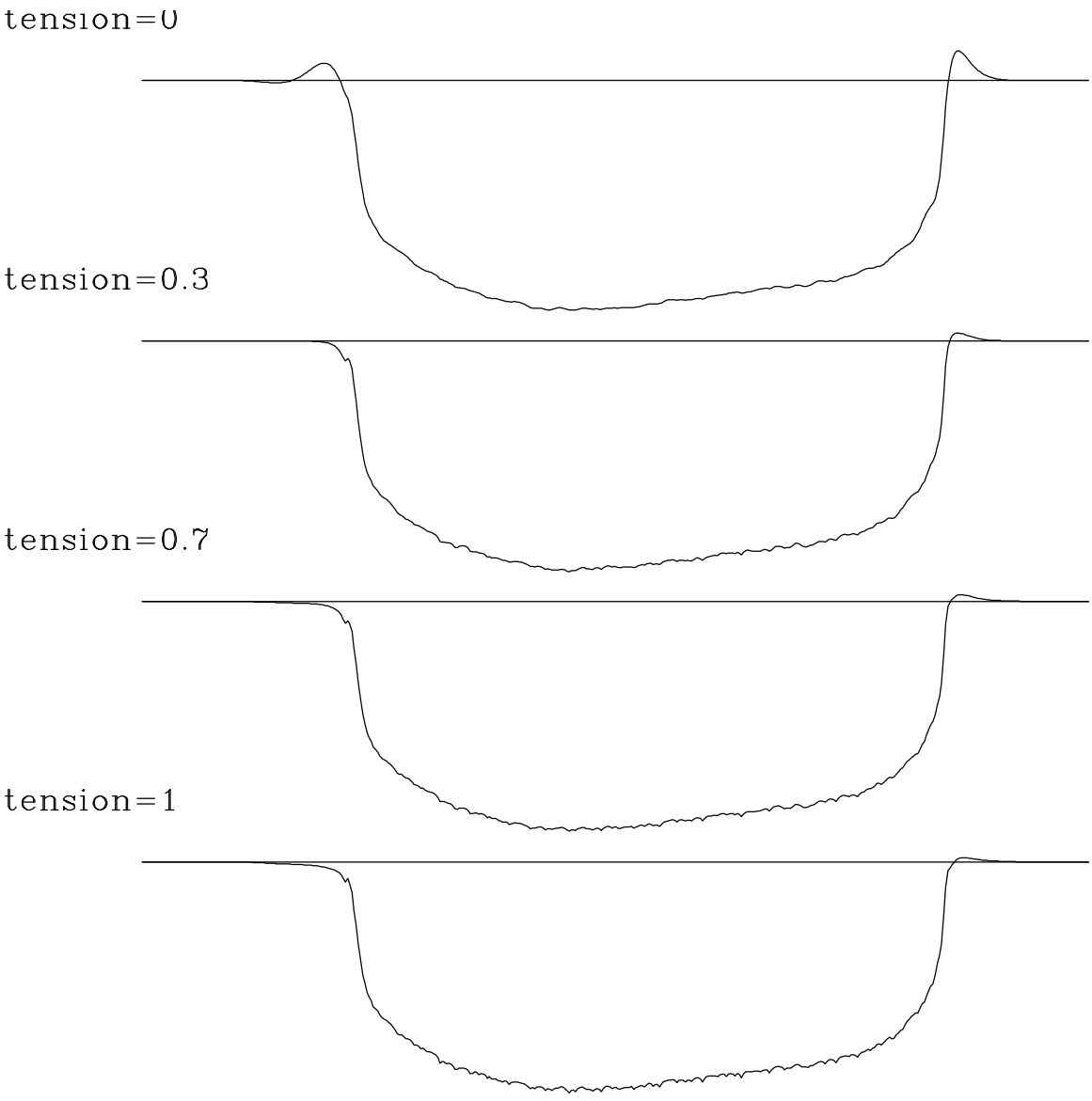

Figure 1.8: Cross-sections of the Sea of Galilee dataset after missing-data interpolation with helical preconditioning. Different plots correspond to different values of the tension parameter. regul-cross [ER]

model is a very convenient representation of seismic data. Unfortunately, early experiences with applying plane-wave destructors for interpolating spatially aliased data showed that they performed poorly in comparison with that of industry-standard F-X prediction-error filters (Spitz, 1991).

For each given frequency, an F-X prediction-error filter (PEF) can be thought of as a Z-transform polynomial. The roots of the polynomial correspond precisely to predicted plane waves (Canales, 1984). Therefore, F-X PEFs simply represent a spectral (frequency-domain) approach to plane-wave destruction. This powerful and efficient approach is, however, not theoretically adequate when the plane-wave slopes or the boundary conditions vary both spatially and temporally.

Multidimensional T-X prediction-error filters (Claerbout, 1992, 1999) share the same purpose of predicting local plane waves. They work well with spatially aliased data and allow for both temporal and spatial variability of the slopes. In practice, however, T-X filters appear as very mysterious objects, because their construction involves many non-intuitive parameters. The user needs to choose a raft of parameters, such as the number of filter coefficients, the gap and the exact shape of the filter, the size, number, and shape of local patches for filter estimation, the number of iterations, and the amount of regularization. Recently developed techniques for handling non-stationary PEFs (Crawley et al., 1998, 1999; Clapp et al., 1999; Crawley, 1999), have demonstrated an excellent performance in a variety of applications (Brown et al., 1999; Clapp and Brown, 2000; Crawley, 2000), but the large number of adjustable parameters still requires a significant level of human interaction and remains the drawback of the method.

Clapp et al. (1997) have recently revived the original plane-wave destructors for preconditioning tomographic problems with a predefined dip field (Clapp et al., 1998; Clapp and Biondi, 1998, 2000). The filters were named *steering filters* because of their ability to steer the solution in the direction of the local dips.

In this section, I revisit Claerbout's original technique of finite-difference plane-wave destruction. First, I develop an approach for increasing the accuracy and dip bandwidth of the

method. Applying the improved filter design to several data regularization problems, I discover that the finite-difference filters often perform as well as or even better than T-X PEFs. At the same time, they keep the number of adjustable parameters to a minimum, and the only quantity we estimate has a clear physical meaning of the local plane-wave slope.

High-order plane-wave destructors

Following the physical model of local plane waves, we can define the mathematical basis of the plane-wave destructor filters as the local plane differential equation

$$\frac{\partial P}{\partial x} + \sigma \frac{\partial P}{\partial t} = 0 \,, \tag{1.8}$$

where $P(t,x)$ is the wave field, and σ is the local slope, which may also depend on t and x. In the case of a constant slope, equation (1.8) has the simple general solution

$$P(t,x) = f(t - \sigma x) \,, \tag{1.9}$$

where $f(t)$ is an arbitrary waveform. Equation (1.9) is nothing more than a mathematical description of a plane wave.

If the slope σ does not depend on t, we can transform equation (1.8) to the frequency domain, where it takes the form of the ordinary differential equation

$$\frac{d\hat{P}}{dx} + i\omega\sigma\,\hat{P} = 0 \tag{1.10}$$

and has the general solution

$$\hat{P}(x) = \hat{P}(0)e^{i\omega\sigma x} \,, \tag{1.11}$$

where $\hat{P}$ is the Fourier transform of P. The complex exponential term in equation (1.11) simply represents a shift of a t-trace according to the slope σ and the trace separation x.

In the frequency domain, the operator for transforming the trace at position $x-1$ to the

neighboring trace at position x is a multiplication by $e^{i\omega\sigma}$. In other words, a plane wave can be perfectly predicted by a two-term prediction-error filter in the F-X domain:

$$a_0\,\hat{P}(x)+a_1\,\hat{P}(x-1)=0\,, \tag{1.12}$$

where $a_0=1$ and $a_1=-e^{-i\omega\sigma}$. The goal of predicting several plane waves can be accomplished by cascading several two-term filters. In fact, any F-X prediction-error filter represented in the Z-transform notation as

$$A(Z_x)=1+a_1Z_x+a_2Z_x^2+\cdots+a_NZ_x^N \tag{1.13}$$

can be factored into a product of two-term filters:

$$A(Z_x)=\left(1-\frac{Z_x}{Z_1}\right)\left(1-\frac{Z_x}{Z_2}\right)\cdots\left(1-\frac{Z_x}{Z_N}\right)\,, \tag{1.14}$$

where $Z_1,Z_2,\ldots,Z_N$ are the zeroes of polynomial (1.13). According to equation (1.12), the phase of each zero corresponds to the slope of a local plane wave multiplied by the frequency. Zeroes that are not on the unit circle carry an additional amplitude gain not included in equation (1.10).

In order to incorporate time-varying slopes, we need to return to the time domain and look for an appropriate analog of the phase-shift operator (1.11) and the plane-prediction filter (1.12). An important property of plane-wave propagation across different traces is that the total energy of the transmitted wave stays invariant throughout the process. This property is assured in the frequency-domain solution (1.11) by the fact that the spectrum of the complex exponential $e^{i\omega\sigma}$ is equal to one. In the time domain, we can reach an equivalent effect by using an all-pass digital filter. In the Z-transform notation, convolution with an all-pass filter takes the form

$$\hat{P}_{x+1}(Z_t)=\hat{P}_x(Z_t)\frac{B(Z_t)}{B(1/Z_t)}\,, \tag{1.15}$$

where $\hat{P}_x(Z_t)$ denotes the Z-transform of the corresponding trace, and the ratio $B(Z_t)/B(1/Z_t)$ is an all-pass digital filter approximating the time-shift operator (1.12). In finite-difference

terms, equation (1.15) represents an implicit finite-difference scheme for solving equation (1.8) with the initial conditions at a constant x. The coefficients of filter $B(Z_t)$ can be determined, for example, by fitting the filter frequency response at small frequencies to the response of the phase-shift operator. The Taylor series technique (equating the coefficients of the Taylor series expansion around zero frequency) yields the expression

$$B_3(Z_t) = \frac{(1-\sigma)(2-\sigma)}{12} Z_t^{-1} + \frac{(2+\sigma)(2-\sigma)}{6} + \frac{(1+\sigma)(2+\sigma)}{12} Z_t \tag{1.16}$$

for a three-point centered filter $B_3(Z_t)$ and the expression

$$\begin{aligned} B_5(Z_t) \;=\; & \frac{(1-\sigma)(2-\sigma)(3-\sigma)(4-\sigma)}{1680} Z_t^{-2} + \frac{(4-\sigma)(2-\sigma)(3-\sigma)(4+\sigma)}{420} Z_t^{-1} + \\ & \frac{(4-\sigma)(3-\sigma)(3+\sigma)(4+\sigma)}{280} + \\ & \frac{(4-\sigma)(2+\sigma)(3+\sigma)(4+\sigma)}{420} Z_t + \frac{(1+\sigma)(2+\sigma)(3+\sigma)(4+\sigma)}{1680} Z_t^2 \end{aligned} \tag{1.17}$$

for a five-point centered filter $B_5(Z_t)$. It is easy to generalize these expressions to longer filters. Figure 1.9 shows the phase of the all-pass filters $B_3(Z_t)/B_3(1/Z_t)$ and $B_5(Z_t)/B_5(1/Z_t)$ for two values of the slope σ in comparison with the exact linear function of equation (1.11). As expected, the phases match the exact line at low frequencies, and the accuracy of the approximation increases with the length of the filter.

Figure 1.9: Phase of the implicit finite-difference shift operators in comparison with the exact solution. The left plot corresponds to $\sigma = 0.5$, the right plot to $\sigma = 0.8$. regul-phase [CR]

In two dimensions, equation (1.15) transforms to the prediction equation analogous to (1.12) with the 2-D prediction filter

$$A(Z_t, Z_x) = 1 - Z_x \frac{B(1/Z_t)}{B(Z_t)} \,. \tag{1.18}$$

In order to characterize several plane waves, we can cascade several filters of the form (1.18) in a manner similar to that of equation (1.14). In the examples of this chapter, I use a modified version of the filter $A(Z_t, Z_x)$, namely the filter

$$C(Z_t, Z_x) = A(Z_t, Z_x)B(Z_t) = B(Z_t) - Z_x B(1/Z_t) \,, \tag{1.19}$$

which avoids the need for polynomial division. In case of the 3-point filter (1.16), the 2-D filter (1.19) has exactly six coefficients, with the second t column being a reversed copy of the first column. When filter (1.19) is used in data regularization problems, it can occasionally cause undesired high-frequency oscillations in the solution, resulting from the near-Nyquist zeroes of the polynomial $B(Z_t)$. The oscillations are easily removed in practice with appropriate low-pass filtering.

In the next subsection, I address the problem of estimating the local slope σ with filters having form (1.19). Estimating the slope is a necessary step for applying the finite-difference plane-wave filters on real data.

Slope estimation

Let us denote by $\mathbf{C}(\sigma)$ the operator of convolving the data with the 2-D filter $C(Z_t, Z_x)$ of equation (1.19) assuming the local slope σ. In order to determine the slope, we can define the least-squares goal

$$\mathbf{C}(\sigma)\,\mathbf{d} \approx 0 \,, \tag{1.20}$$

where $\mathbf{d}$ is the known data and the approximate equality implies that the solution is found by minimizing the power of the left-hand side. Equations (1.16) and (1.17) show that the slope σ enters in the filter coefficients in an essentially non-linear way. However, one can still apply

the linear iterative optimization methods by an analytical linearization of equation (1.20). The linearization (also known as the Newton iteration) implies solving the linear system

$$\mathbf{C}'(\sigma_0)\,\Delta\sigma\,\mathbf{d} + \mathbf{C}(\sigma_0)\,\mathbf{d} \approx 0 \tag{1.21}$$

for the slope increment $\Delta\sigma$. Here σ_0 is the initial slope estimate, and $\mathbf{C}'(\sigma)$ is a convolution with the filter, obtained by differentiating the filter coefficients of $\mathbf{C}(\sigma)$ with respect to σ. After system (1.21) is solved, the initial slope σ_0 is updated by adding $\Delta\sigma$ to it, and one can solve the linear problem again. Depending on the starting solution, the method may require several non-linear iterations to achieve an acceptable convergence. The described linearization approach is similar in idea to tomographic velocity estimation (Nolet, 1987).

In the case of a time- and space-varying slope σ, system (1.21) may lead to undesirably rough slope estimates. Moreover, the solution will be undefined in regions of unknown or constant data. Both these problems are solved by adding a regularization (styling) goal to system (1.21). The additional goal takes the form analogous to (**??**):

$$\epsilon\mathbf{D}\,\Delta\sigma \approx 0\,, \tag{1.22}$$

where $\mathbf{D}$ is an appropriate roughening operator and ϵ is a scaling coefficient. For simplicity, I chose $\mathbf{D}$ to be the gradient operator. An alternative choice would be to treat local dips as smooth data and to apply to them the tension-spline preconditioning technique from the previous section.

In theory, estimating two different slopes σ_1 and σ_2 from the available data is only marginally more complicated than estimating a single slope. The convolution operator becomes a cascade of $\mathbf{C}(\sigma_1)$ and $\mathbf{C}(\sigma_2)$, and the linearization yields

$$\mathbf{C}'(\sigma_1)\mathbf{C}(\sigma_2)\,\Delta\sigma_1\,\mathbf{d} + \mathbf{C}(\sigma_1)\mathbf{C}'(\sigma_2)\,\Delta\sigma_2\,\mathbf{d} + \mathbf{C}(\sigma_1)\mathbf{C}(\sigma_2)\,\mathbf{d} \approx 0\,. \tag{1.23}$$

The regularization condition should now be applied to both $\Delta\sigma_1$ and $\Delta\sigma_2$:

$$\epsilon \mathbf{D}\, \Delta\sigma_1 \approx 0\,; \tag{1.24}$$

$$\epsilon \mathbf{D}\, \Delta\sigma_2 \approx 0\,. \tag{1.25}$$

The solution will obviously depend on the initial values of σ_1 and σ_2, which should not be equal to each other. System (1.23) is generally underdetermined, because it contains twice as many estimated parameters as equations, but an appropriate choice of the starting solution and the additional regularization (1.24-1.25) allow us to arrive at a practical solution.

The application examples of the next subsection demonstrate that when the system of equations (1.23-1.22) or (1.23-1.25) are optimized in the least-squares sense in a cycle of several linearization iterations, it leads to smooth and reliable slope estimates. The regularization conditions (1.22) and (1.24-1.25) assure a smooth extrapolation of the slope to the regions of unknown or constant data.

Examples of data regularization

In this subsection, I examine the performance of the finite-difference plane-destruction filters on several test applications.

Gap interpolation

Missing-data interpolation was introduced in Chapter **??** as a simple case of data regularization when the input data are already binned to regular grid locations but with remaining uncovered gaps.

Figure 1.10 shows a simple synthetic example of gap interpolation from Claerbout (1999). The input data has a large elliptic gap cut out in a two plane-wave model. I estimate both dip components from the input data by using the method of equations (1.23-1.25). The initial values for the two local dips were 1 and 0, and the estimated values are close to the true dips of 2 and -1 (the third and fourth plots in Figure 1.10.) Although the estimation program

does not make any assumption about dip being constant, it correctly estimates nearly constant values with the help of regularization equations (1.24-1.25). The rightmost plot in Figure 1.10 shows the result of gap interpolation with a two-plane local plane-wave destructor. The result is nearly ideal and compares favorably with the analogous result of the T-X PEF technique (Claerbout, 1999).

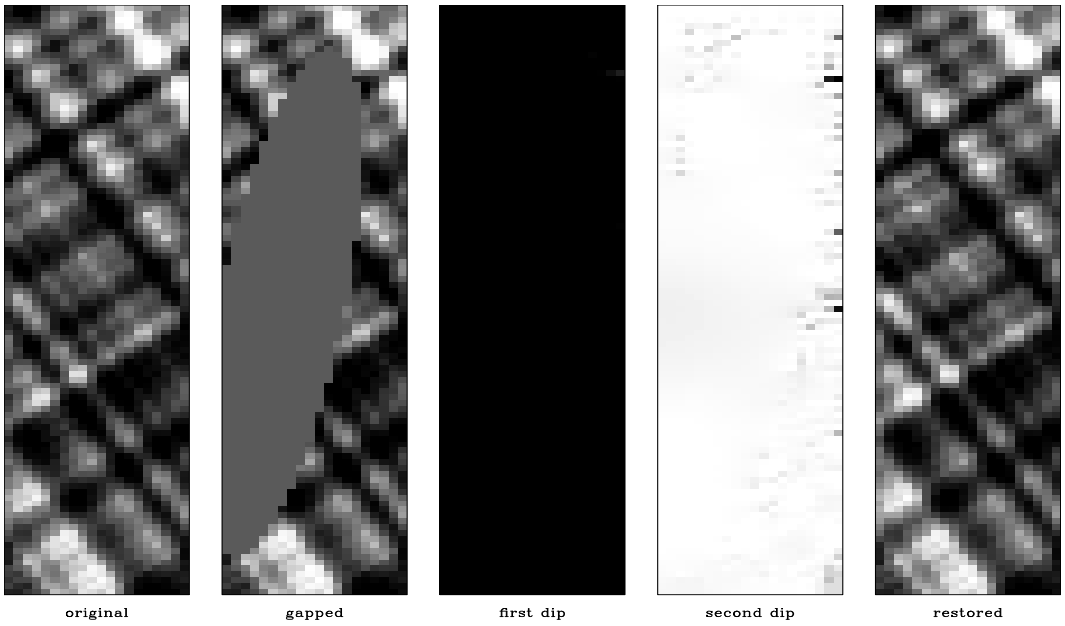

Figure 1.10: Synthetic gap interpolation example. From left to right: original data, input data, first estimated dip, second estimated dip, interpolation output. regul-hole [ER]

Figure 1.11 is another benchmark gap interpolation example from Claerbout (1999), already featured in Chapter **??** (Figures **??**-**??**). The data are ocean-depth measurements from one day SeaBeam acquisition. The data after normalized binning are shown in the left plot of Figure 1.11. From the known part of the data, we can partially see a certain elongated and faulted structure on the ocean floor created by fractures around an ocean ridge. Estimating a smoothed dominant dip in the data and interpolating with the plane-wave destructor filters produces the image in the right plot of Figure 1.11. The V-shaped acquisition pattern is somewhat visible in the interpolation result, which might indicate the presence of a fault. Otherwise, the result is both visually pleasing and in full agreement with the input data. Clapp (2000b) uses the same data example to obtain multiple statistically equivalent realizations of

the interpolated data.

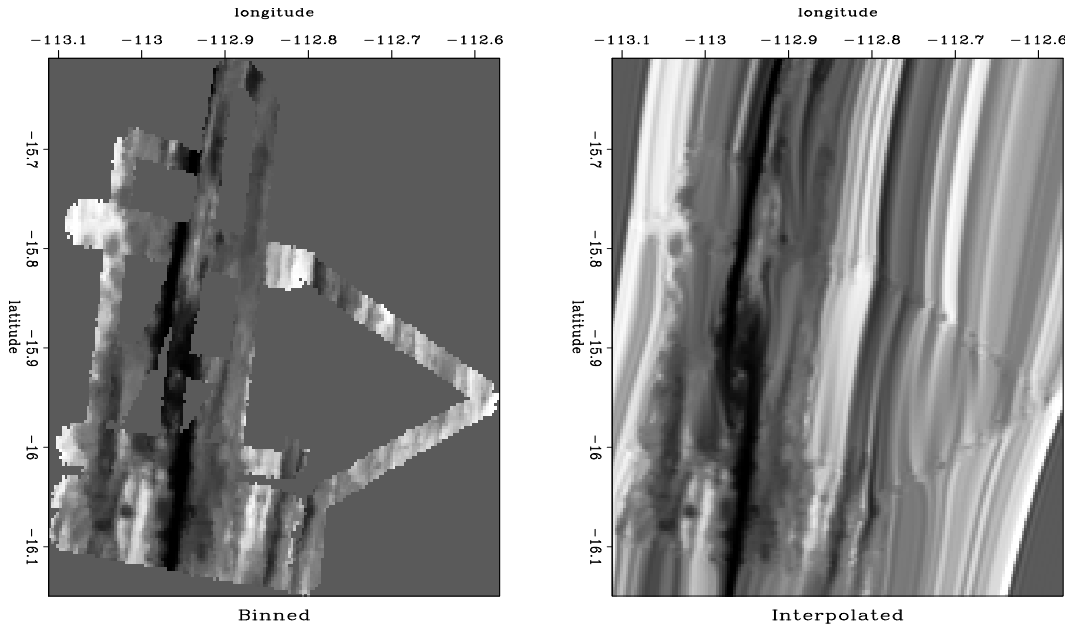

Figure 1.11: Depth of the ocean from SeaBeam measurements. Left plot: after binning. Right plot: after binning and gap interpolation. regul-seab [ER,M]

A 3-D interpolation example is shown in Figure 1.12. The input data resulted from a passive seismic experiment (Cole, 1995) and originally contained many gaps because of instrument failure. I interpolated the 3-D gaps with a pair of two orthogonal plane-wave destructors in the manner proposed by Schwab and Claerbout (1995) for T-X prediction filters. The interpolation result shows a visually pleasing continuation of locally plane events through the gaps. It compares favorably with an analogous result of a stationary T-X PEF.

We can conclude that plane-wave destructors provide an effective method of gap filling and missing-data interpolation.

Trace interpolation beyond aliasing

Spitz (1991) popularized the application of prediction-error filters to regular trace interpolation and showed how the spatial aliasing restriction can be overcome by scaling the frequencies of F-X PEFs. An analogous technique for T-X filters was developed by Claerbout (1992, 1999)

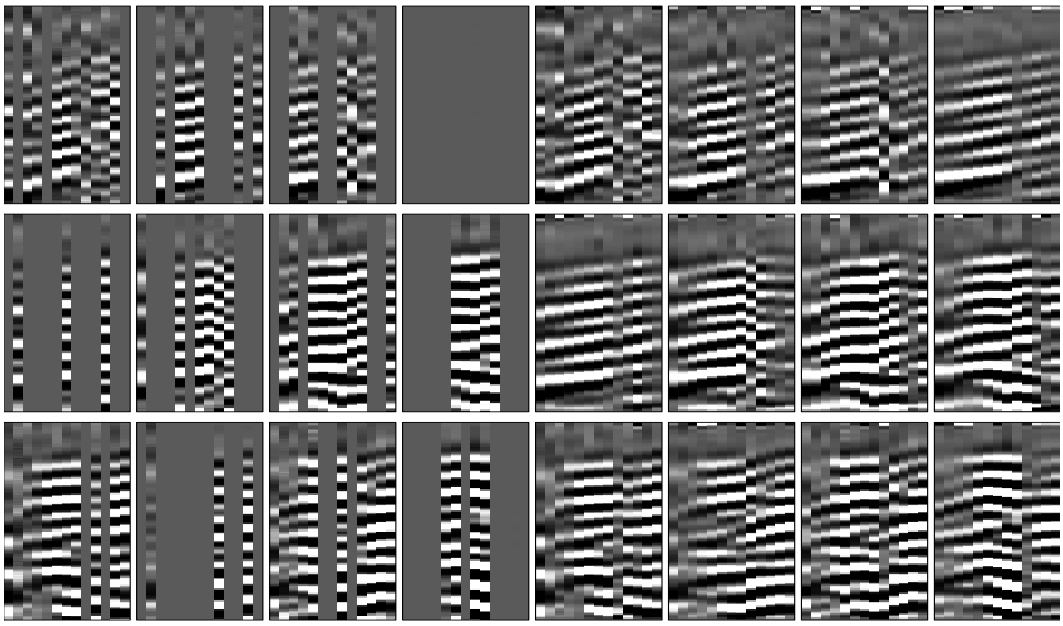

Figure 1.12: 3-D gap interpolation in passive seismic data. The left 12 panels are slices of the input data. The right 12 panels are the corresponding slices in the interpolation output. regul-passfill [ER,M]

and was applied for 3-D interpolation with non-stationary PEFs by Crawley (2000). The T-X technique implies stretching the filter in all directions so that its dip spectrum is preserved while the coefficients can be estimated at alternating traces. After the filter is estimated, it is scaled back and used for interpolating missing traces between the known ones. A similar method works for finite-difference plane wave destructors, only we need to take special care to avoid aliased dips at the dip estimation stage.

A simple synthetic example of interpolation beyond aliasing is shown in Figure 1.13. The input data are clearly aliased and non-stationary. To take the aliasing into account, I estimate the two dips present in the data with the slope estimation technique of the previous subsection. The first dip corresponds to the true slope, while the second dip corresponds to the aliased dip component. In this example, the true dip is non-negative everywhere and is easily distinguished from the aliased one. Throwing away the aliased dip and interpolating intermediate traces with the true dip produces the accurate interpolation result shown in the right plot of Figure 1.13.

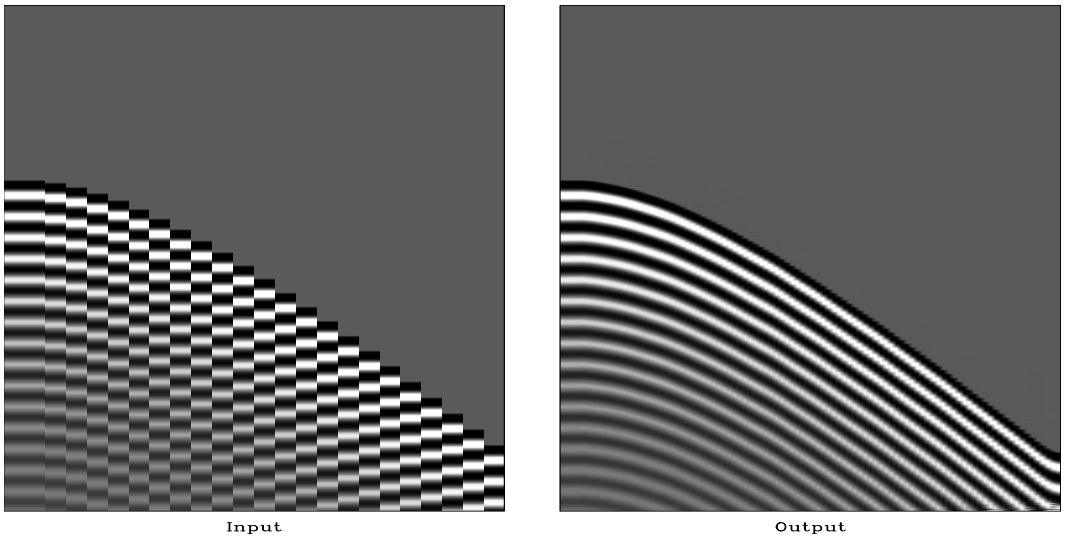

Figure 1.13: Synthetic example of interpolation beyond aliasing with plane-wave destructor filters. Left: input aliased data, right: interpolation output. regul-aliasp2 [ER]

Figure 1.14 shows a marine 2-D shot gather from a deep water Gulf of Mexico survey before and after subsampling in the offset direction. The data are similar to those used by Crawley (2000). The shot gather has long-period multiples and complicated diffraction events caused by a salt body. The amplitudes of the hyperbolic events are not as uniformly distributed as in the synthetic case of Figure 1.13. Subsampling by a factor of two (the right plot in Figure 1.14) causes a clearly visible aliasing in the steeply dipping events. The goal of the experiment is to interpolate the missing traces in the subsampled data and to compare the result with the original gather shown in the left plot of Figure 1.14.

A straightforward application of the dip estimation equations (1.23-1.25) applied to aliased data can easily lead to erroneous aliased dip estimation. In order to avoid this problem, I chose a slightly more complex strategy. The algorithm for trace interpolation of aliased data consists of the following steps:

1. Applying Claerbout's T-X methodology, stretch a two-dip plane-wave destructor filter and estimate the dips from decimated data.

2. The second estimated dip will be degraded by aliasing. Ignore this initial second-dip

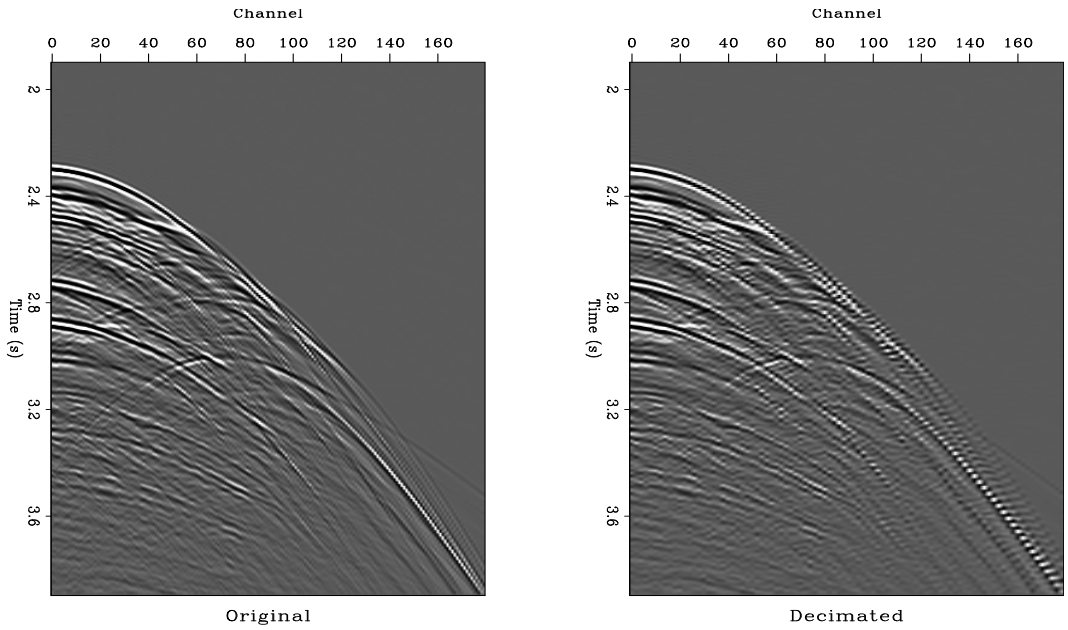

Figure 1.14: 2-D marine shot gather. Left: original. Right: subsampled by a factor of two in the offset direction. regul-sean2 [ER]

estimate.

3. Estimate the second dip component again by fixing the first dip component and using it as the initial estimate of the second component. This trick prevents the nonlinear estimation algorithm from picking the wrong (aliased) dip in the data.

4. Downscale the estimated two-dip filter and use it for interpolating missing traces.

The two estimated dip components are shown in Figure 1.15. The first component contains only positive dips. The second component coincides with the first one in the areas where only a single dip is present in the data. In other areas, it picks the complementary dip, which has a negative value for back-dipping hyperbolic diffractions.

Figure 1.16 shows the interpolation result and the difference between the interpolated traces and the original traces, plotted at the same clip value. The method succeeded in the sense that it is impossible to distinguish interpolated traces from the interpolation result alone. However, it is not ideal, because some of the original energy is missing in the output. A

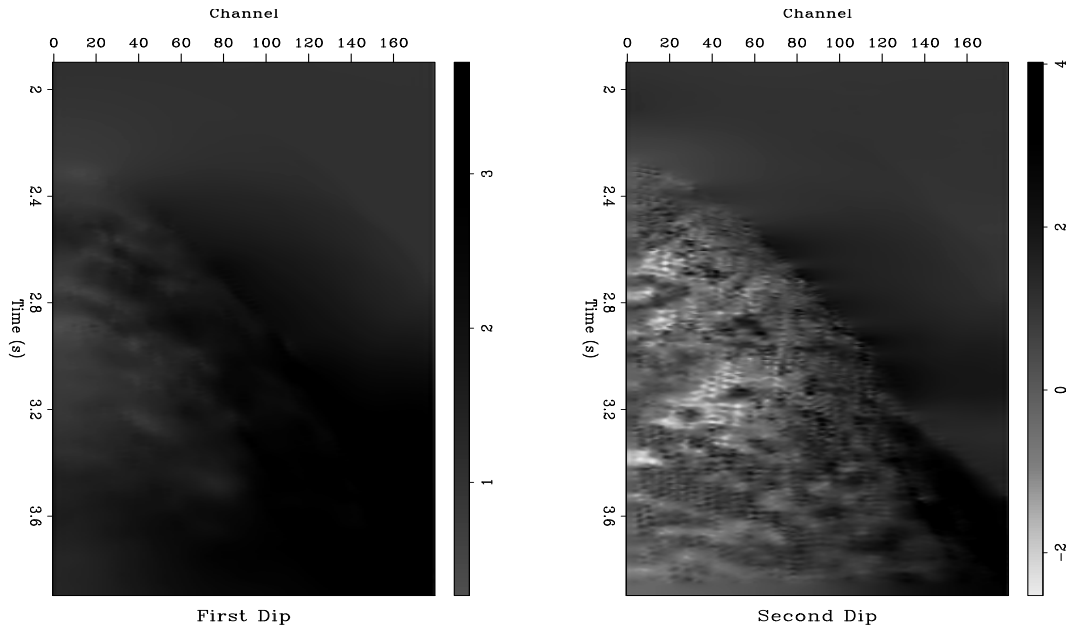

Figure 1.15: Two components of the estimated dip field for the decimated 2-D marine shot gather. regul-sean2-dip [ER]

close-up comparison between the original and the interpolated traces in Figure 1.17 shows that imperfection in more detail. Some of the steepest events in the middle of the section are poorly interpolated, and in some of the other places, the second dip component is continued instead of the first one.

One could improve the interpolation result considerably by including another dimension. To achieve a better result, we can use a pair of plane-wave destructors, one predicting local plane waves in the offset direction and the other predicting local plane waves in the shot direction.

Plane-wave destruction and B-splines

The general method of B-spline regularization, outlined in Chapter **??**, is easily applicable for the case of local plane-wave destruction. The continuous regularization operator D in this case comes from the theoretical plane-wave differential equation (1.8). We simply need

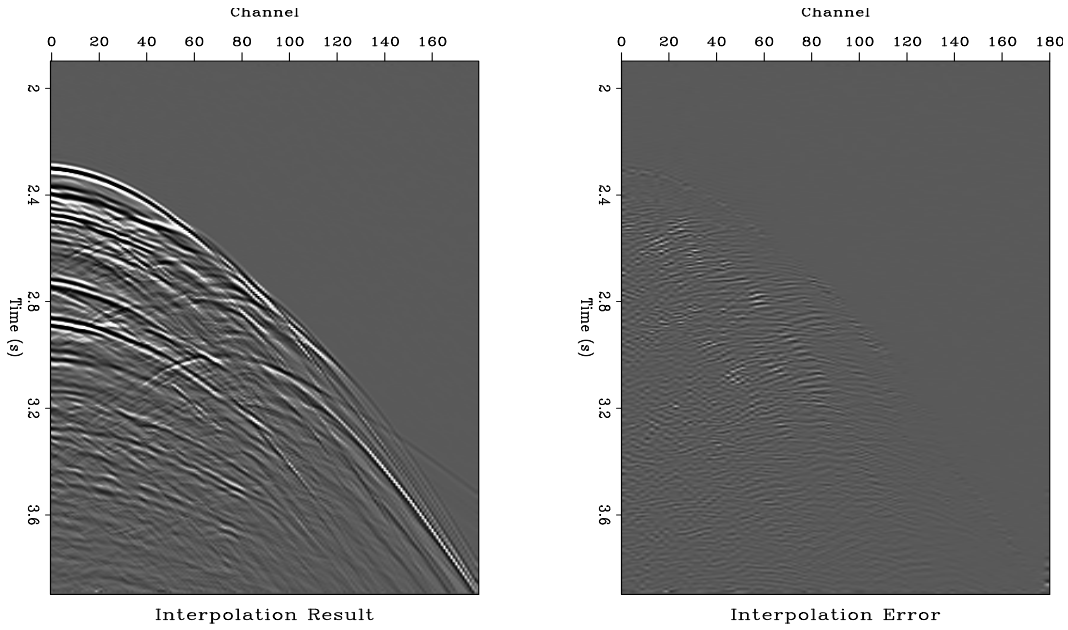

Figure 1.16: Left: 2-D marine shot gather after trace interpolation. Right: Difference between the interpolated and the original gather. regul-sean2-int [ER]

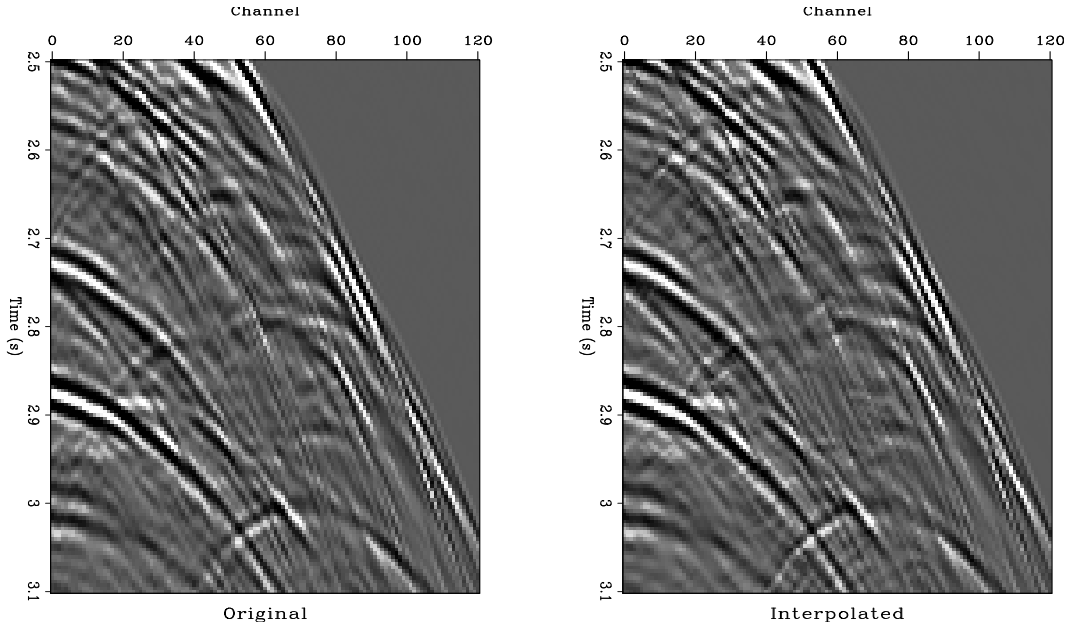

Figure 1.17: Close-up comparison of the interpolated (right) and the original data (left). regul-sean2-close [ER,M]

to construct the auto-correlation filter d_j according to formula (**??**) and factorize it with the Wilson-Burg method. Figure 1.18 shows three plane waves constructed from three distant spikes by application of inverse recursive filtering with two different B-spline regularizers. The left plot was obtained with first-order B-splines (equivalent to linear interpolation). This type of regularizer is identical to Clapp's steering filters (Clapp et al., 1997) and suffers from numerical dispersion effects. The right plot was obtained with third-order splines. Most of the dispersion is suppressed by using a more accurate interpolation.

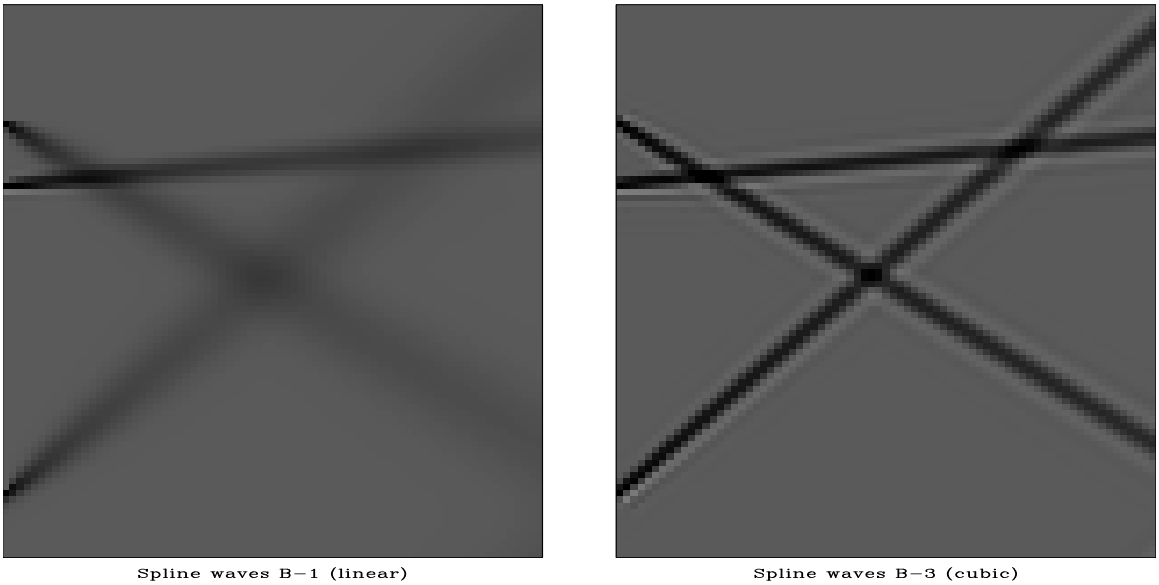

Figure 1.18: B-spline plane-wave regularization. Three plane waves are constructed by 2-D recursive filtering with the B-spline plane-wave regularizer. Left: using first-order B-splines (linear interpolation). Right: using third-order B-splines. regul-sthree [ER,M]

Equipped with the powerful B-spline plane-wave construction, we can now approach the main goal of this work: three-dimensional seismic data regularization. For an illustrative test, I chose the North Sea dataset, which was previously used for testing azimuth moveout (Biondi et al., 1998) and common-azimuth migration (Biondi, 1996). Figure **??** in the introduction showed the highly irregular midpoint geometry for a selected in-line and cross-line offset bin in the data. The data irregularity is also evident in the bin fold map, shown in Figure 1.19. The goal of data regularization is to create a regular data cube at the specified bins from the irregular input data, which have been preprocessed by normal moveout.

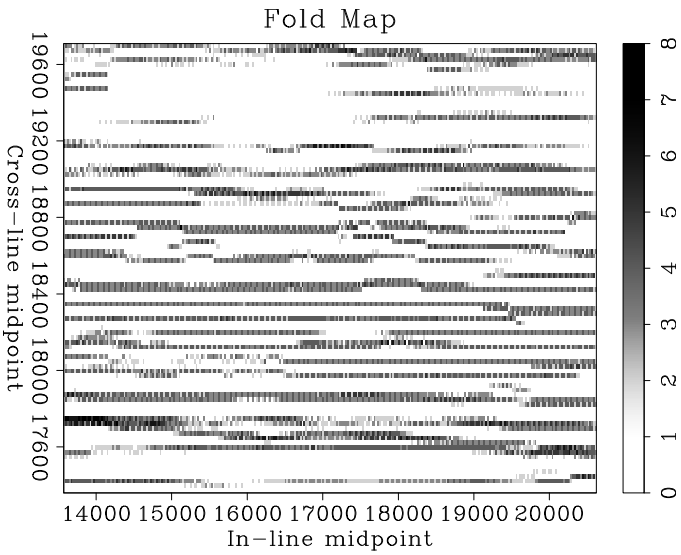

Figure 1.19: Map of the fold distribution for the 3-D data test. regul-fold-win [ER]

The data cube after normalized binning is shown in Figure 1.20. Binning works reasonably well in the areas of large fold but fails to fill the zero fold gaps and has an overall limited accuracy.

For efficiency, I perform regularization on individual time slices. Figure 1.21 shows the result of regularization using bi-linear interpolation and smoothing preconditioning with the minimum-phase Laplacian filter. The empty bins are filled in a consistent manner but the data quality is distorted because simple smoothing fails to characterize the complicated data structure. Instead of continuous events, we see smoothed blobs in the time slices. The events in the in-line and cross-line sections are also not clearly pronounced.

We can use the smoothing regularization result to estimate the local dips in the data, design invertible local plane-wave destruction filters, and repeat the regularization process. Inverse interpolation using bi-linear interpolations with plane-wave preconditioning is shown in Figure 1.22. The regularization result is improved: the continuous reflection events become clearly visible in the time slices. As expected, a higher quality result is achieved with cubic B-spline (Figure 1.23). Regularization works again in constant time slices, using recursive filter preconditioning with plane-wave destructor filters analogous to those in Figure 1.18. Despite the irregularities in the input data, the regularization result preserves both flat reflection events and steeply-dipping diffractions. Preserving diffractions is important for correct imaging of

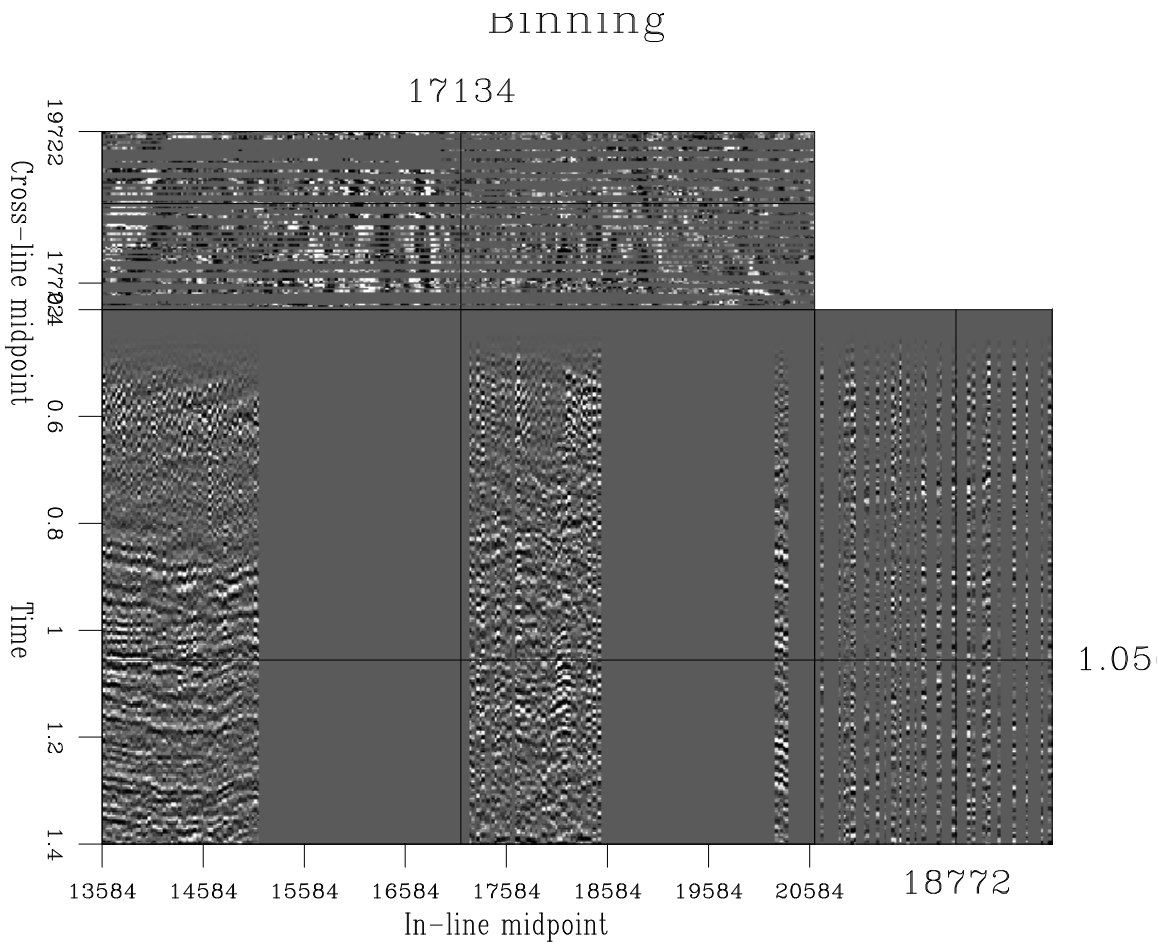

Figure 1.20: 3-D data after normalized binning. regul-bin-win [CR]

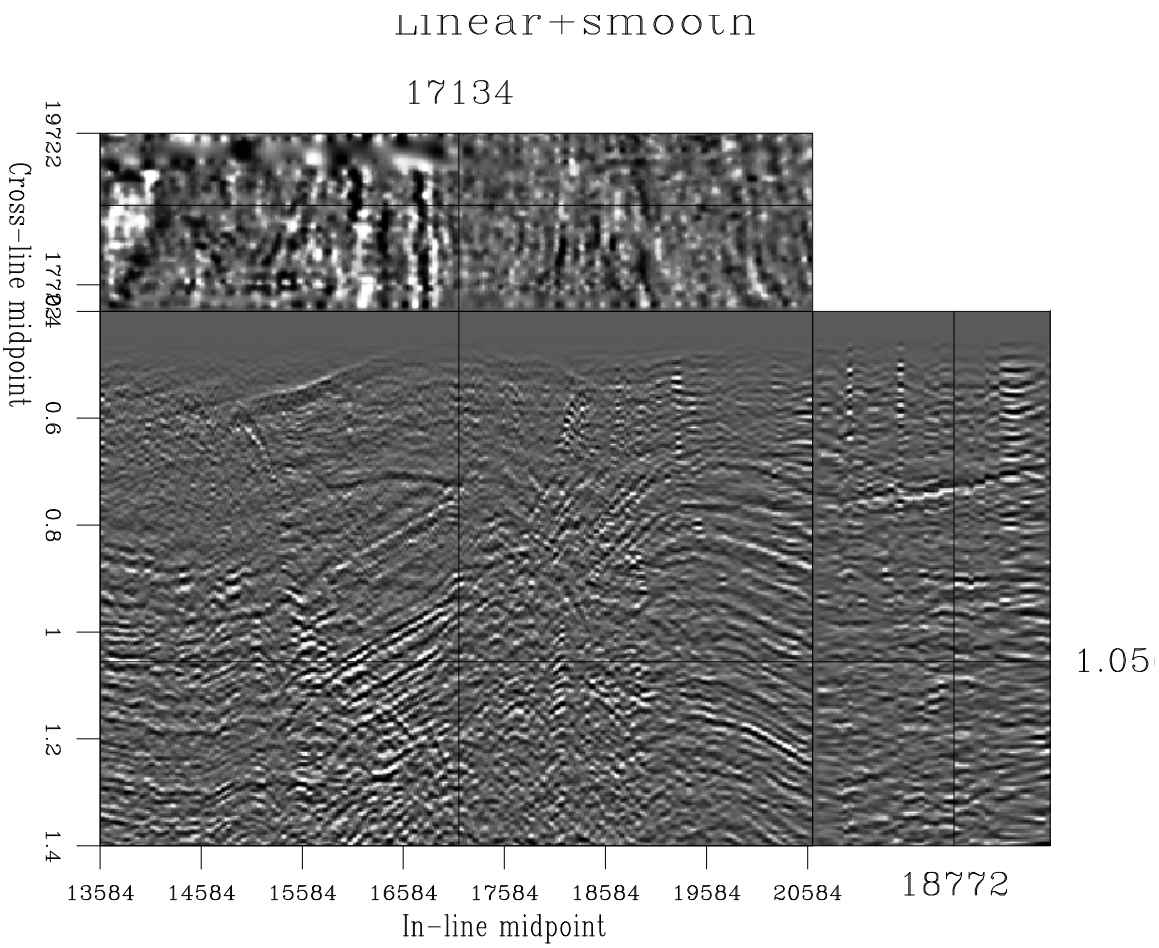

Figure 1.21: 3-D data regularized with bi-linear interpolation and smoothing preconditioning. regul-smo2-win [CR]

sharp edges in the subsurface structure (Biondi and Palacharla, 1996).

For simplicity, I assumed only a single local dip component in the data. This assumption degrades the result in the areas of multiple conflicting dips, such as the intersections of plane reflections and hyperbolic diffractions in Figure 1.23. One could improve the regularization result by considering multiple local dips. In the next section of this chapter, I describe an alternative offset-continuation approach, which uses a physical connection between neighboring offsets instead of assuming local continuity in the midpoint domain.

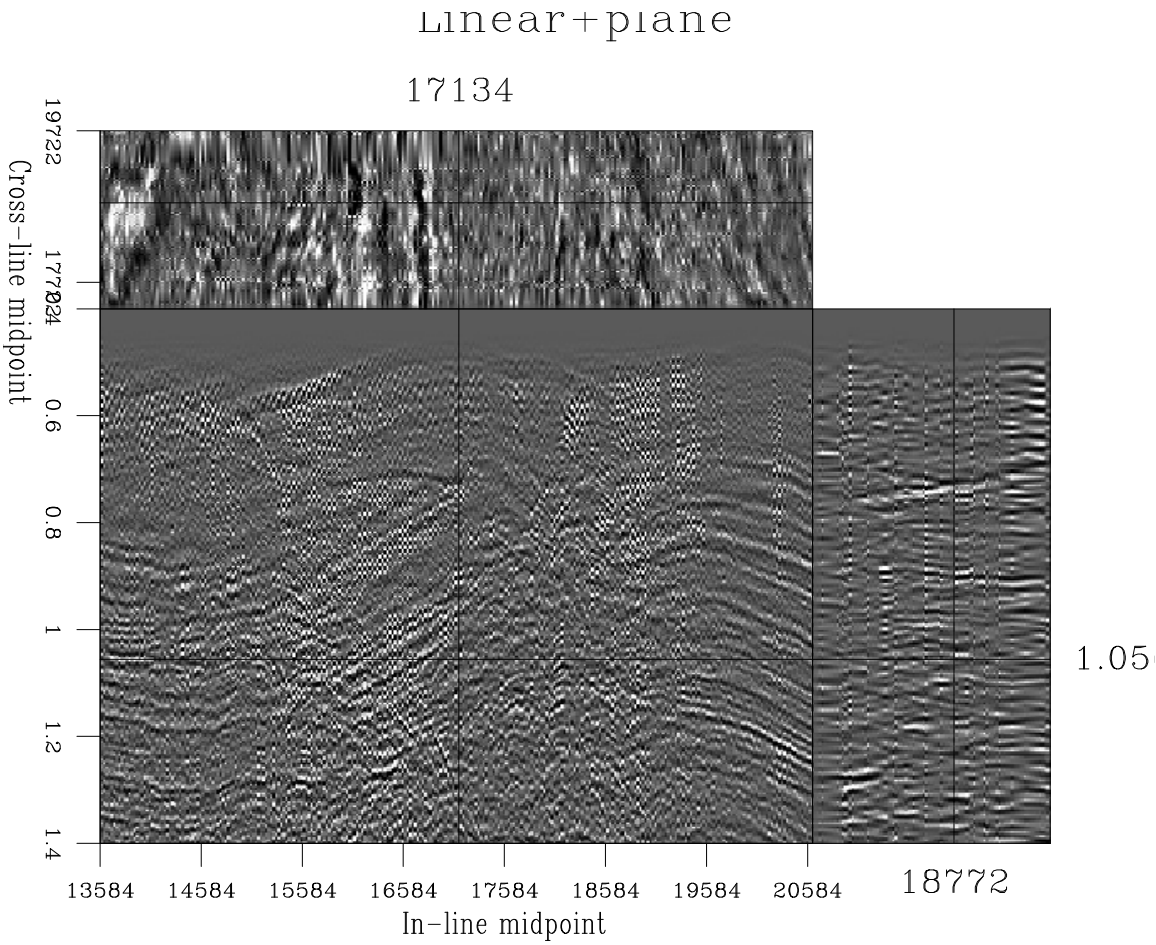

Figure 1.22: 3-D data regularized with bi-linear interpolation and local plane-wave preconditioning. regul-int2-win [CR]

The 3-D results of this subsection were obtained with an efficient 2-D regularization in time slices. This approach is computationally attractive because of its easy parallelization:

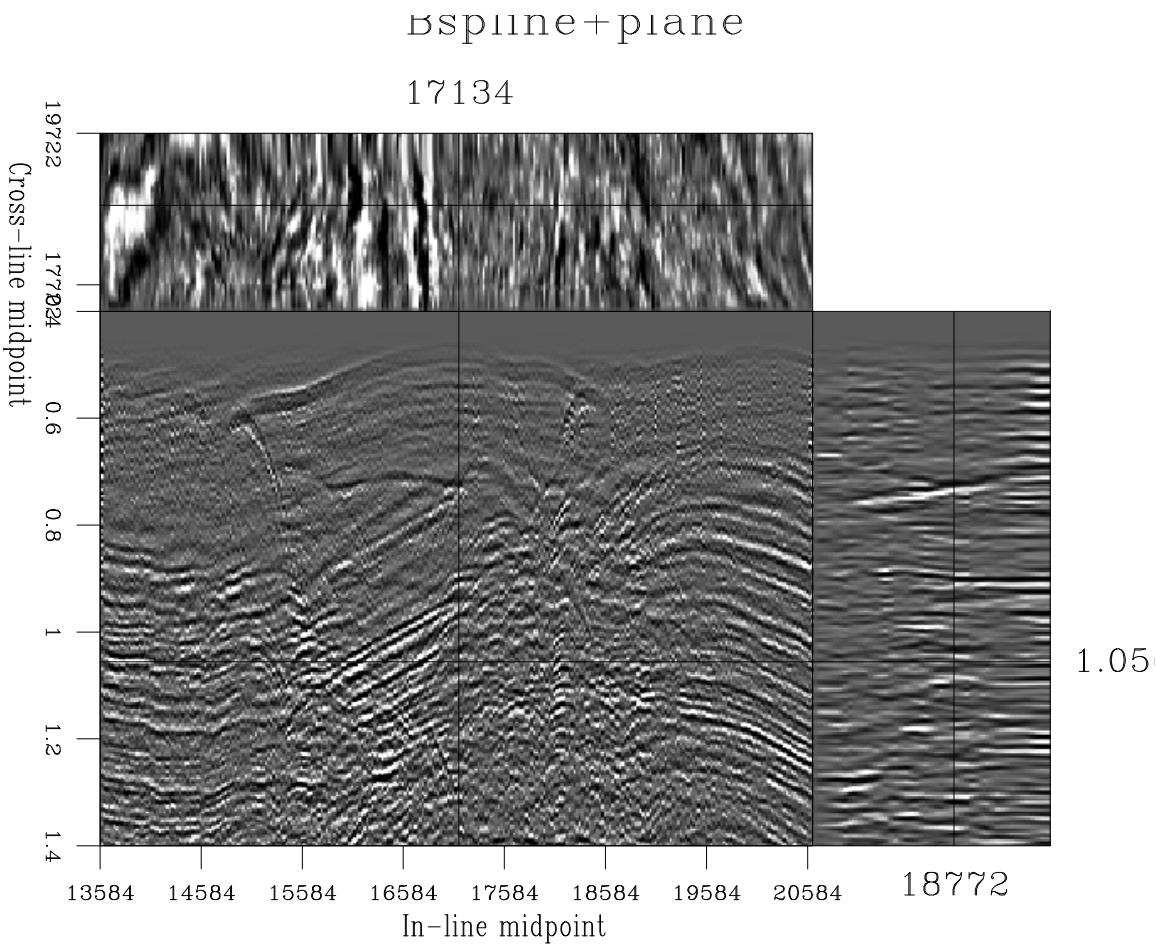

Figure 1.23: 3-D data regularized with cubic B-spline interpolation and local plane-wave preconditioning. regul-int4-win [CR]

different slices can be interpolated independently and in parallel. Figure 1.24 shows the interpolation result for four selected time slices. Local plane waves, barely identifiable after binning (left plots in Figure 1.24), appear clear and continuous in the interpolation result (right plots in Figure 1.24). Different time slices are assembled together to form the 3-D cube shown in Figure 1.23.

A more powerful, although less convenient, approach to 3-D data regularization, is the full 3-D plane-wave destruction. I discuss it in the next subsection.

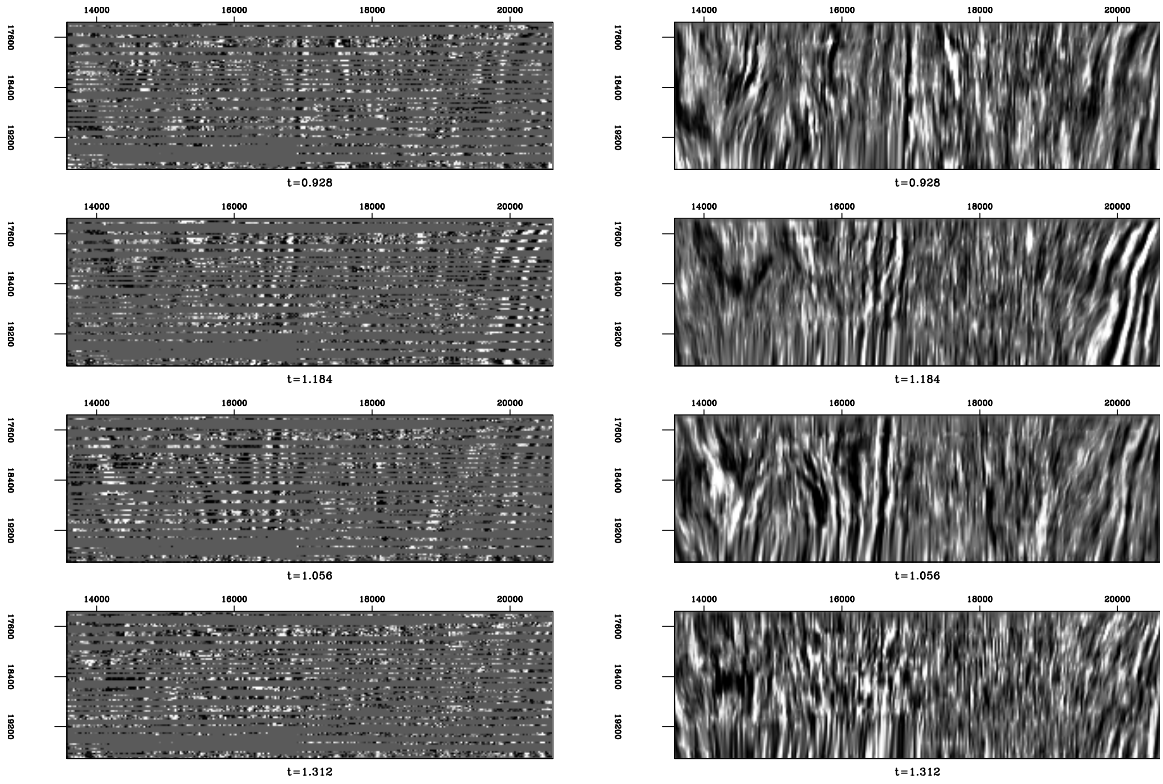

Figure 1.24: Selected time slices of the 3-D dataset. Left: after binning. Right: after plane-wave data regularization. The data regularization program identifies and continues local plane waves in the data. regul-winslice [CR]

Plane-wave destruction in 3-D

The theory of plane-wave prediction in three dimensions is described by Claerbout (1993, 1999). Predicting a local plane wave with T-X filters amounts to finding a pair of two-dimensional filters for two orthogonal planes in the 3-D space. Each of the filters predicts locally straight lines in the corresponding plane. The system of two 2-D filters is sufficient for predicting all but purely vertical plane waves. In the latter case, a third 2-D filter for the remaining orthogonal plane is needed. Schwab (1998) discusses this approach in more detail.

Using two prediction filters implies dealing with two filtering output volumes for each input volume. This situation becomes inconvenient when plane-wave destructors are used for regularizing linear inverse problems. We cannot apply the efficient recursive preconditioning introduced in Chapter **??** unless the regularization operator is square, or, in other words, only one plane-wave destructor is involved.

Helical filtering (Claerbout, 1998a) brings us new tools for addressing this problem. In this subsection, I show how to combine orthogonal 2-D plane predictors into a single three-dimensional filter with similar spectral properties. The 3-D filter can then work for preconditioning 3-D inverse problems, such as data regularization. The construction employs again the Wilson-Burg method of spectral factorization, adapted for multidimensional filtering with the help of the helix transform.

I use simple synthetic examples to demonstrate the applicability of plane-wave prediction to 3-D problems.

Factorizing plane waves

Let us denote the coordinates of a three-dimensional space by t, x, and y. A theoretical plane wave is described by the equation

$$P(t,x,y) = f(t - \sigma_x x - \sigma_y y)\,, \tag{1.26}$$

where f is an arbitrary function, and σ_x and σ_y are the plane slopes in the corresponding direction. It is easy to verify that a plane wave of the form (1.26) satisfies the following system of partial differential equations:

$$\begin{cases} \left(\dfrac{\partial}{\partial x} + \sigma_x \dfrac{\partial}{\partial t}\right) P &= 0 \\ \left(\dfrac{\partial}{\partial y} + \sigma_y \dfrac{\partial}{\partial t}\right) P &= 0 \end{cases} \tag{1.27}$$

The first equation in (1.27) describes plane waves on the $\{t,x\}$ slices and is completely equivalent to equation (1.8). In its discrete form, it is represented as a convolution with the two-dimensional finite-difference filter $\mathbf{C}_x$ from equation (1.19). Similarly, the second equation transforms into a convolution with filter $\mathbf{C}_y$, which acts on the $\{t,y\}$ slices. The discrete (finite-difference) form of equations (1.8) involves a blocked convolution operator:

$$\begin{bmatrix} \mathbf{C}_x \\ \mathbf{C}_y \end{bmatrix} \mathbf{m} = \mathbf{0}\,, \tag{1.28}$$

where $\mathbf{m}$ is the model vector corresponding to $P(t,x,y)$.

As follows from the theoretical analysis of the data regularization problem in Chapter **??**, regularization implicitly deals with the spectrum of the regularization filter, which approximates the inverse model covariance. In other words, it involves the square operator

$$\begin{bmatrix} \mathbf{C}_x^T & \mathbf{C}_y^T \end{bmatrix} \begin{bmatrix} \mathbf{C}_x \\ \mathbf{C}_y \end{bmatrix} = \mathbf{C}_x^T \mathbf{C}_x + \mathbf{C}_y^T \mathbf{C}_y\,. \tag{1.29}$$

If we were able to transform this operator to the form $\mathbf{C}^T\mathbf{C}$, where $\mathbf{C}$ is a three-dimensional minimum-phase convolution, we could use the three-dimensional filter $\mathbf{C}$ in place of the inconvenient pair $\mathbf{C}_x$ and $\mathbf{C}_y$.

The problem of finding $\mathbf{C}$ from its spectrum is the familiar spectral factorization problem. In fact, we already encountered a problem analogous to (1.29) in the previous section in the

factorization of the discrete two-dimensional Laplacian operator:

$$\Delta = \nabla^T \nabla = \left[\begin{array}{cc} \partial_x^T & \partial_y^T \end{array} \right] \left[\begin{array}{c} \partial_x \\ \partial_y \end{array} \right] = \mathbf{H}^T \mathbf{H} \,, \tag{1.30}$$

where ∂_x and ∂_y represent the partial derivative operators along the x and y directions, respectively, and the two-dimensional filter $\mathbf{H}$ is known as *helix derivative* (Claerbout, 1999; Zhao, 1999).

If we represent the filter $\mathbf{C}_x$ with the help of a simple first-order upwind finite-difference scheme

$$P(t,x+1) - P(t,x) + \sigma_x \left[P(t+1,x+1) - P(t,x+1) \right] = 0 \,, \tag{1.31}$$

then, after the helical mapping to 1-D, it becomes a one-dimensional filter with the Z-transform

$$C_x(Z) = 1 - \sigma_x Z^{N_t+1} + (\sigma_x - 1) Z^{N_t} \,, \tag{1.32}$$

where N_t is the number of samples on the t-axis. Similarly, the filter $\mathbf{C}_y$ takes the form

$$C_y(Z) = 1 - \sigma_y Z^{N_t N_x+1} + (\sigma_y - 1) Z^{N_t N_x} \,. \tag{1.33}$$

The problem is reduced to a 1-D spectral factorization of

$$\begin{aligned} C_x(1/Z)C_x(Z) + C_y(1/Z)C_y(Z) = {} & -\sigma_y \tfrac{1}{Z^{N_t N_x+1}} + (\sigma_y - 1)\tfrac{1}{Z^{N_t N_x}} - \\ & \sigma_x \tfrac{1}{Z^{N_t+1}} + (\sigma_x - 1)\tfrac{1}{Z^{N_t-1}} + \left[\sigma_x(1-\sigma_x) + \sigma_y(1-\sigma_y)\right]\tfrac{1}{Z} + \\ & 2 + \sigma_x(\sigma_x - 1) + \sigma_y(\sigma_y - 1) + \left[\sigma_x(1-\sigma_x) + \sigma_y(1-\sigma_y)\right] Z + \\ & (\sigma_x - 1) Z^{N_t-1} - \sigma_x Z^{N_t+1} + (\sigma_y - 1) Z^{N_t N_x} - \sigma_y Z^{N_t N_x+1} \,. \end{aligned} \tag{1.34}$$

The spectral factorization of (1.34) produces a minimum-phase filter applicable for 3-D forward and inverse convolution. Equation (1.34) is shown here just to illustrate the concept. In practice, I use the longer and much more accurate plane-wave filters of equation (1.19) in place of the simplified filters (1.32) and (1.33).

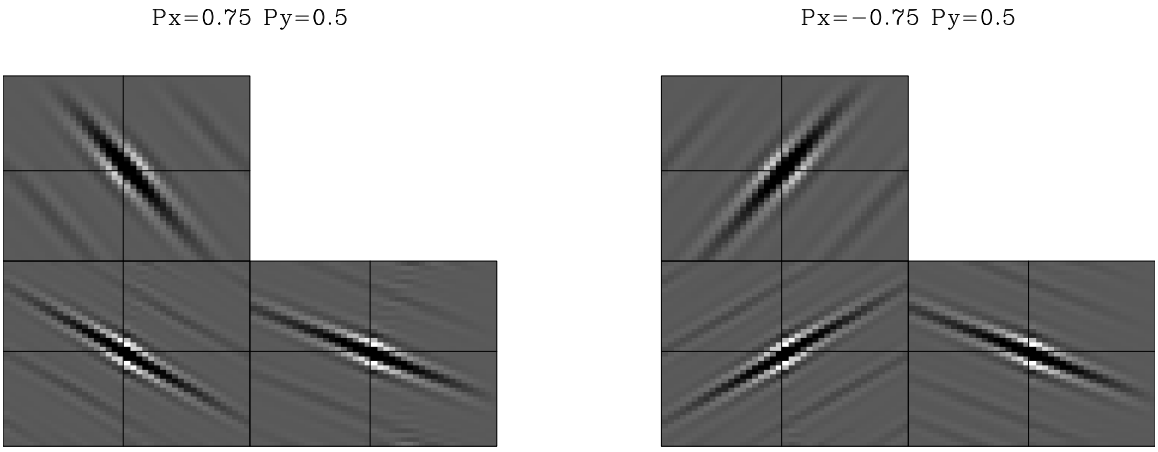

Figure 1.25: 3-D plane wave construction with the factorized 3-D filter. Left: $\sigma_x = 0.75$, $\sigma_y = 0.5$. Right: $\sigma_x = -0.75$, $\sigma_y = 0.5$. regul-cube [ER,M]

Figure 1.25 shows examples of plane-wave construction. The two plots in the figure are outputs of a spike, divided recursively (on a helix) by $\mathbf{C}^T\mathbf{C}$, where $\mathbf{C}$ is a 3-D minimum-phase filter, obtained by the Wilson-Burg factorization.

Clapp (2000a) has proposed constructing 3-D plane-wave destruction (steering) filters by splitting. In Clapp's method, the two orthogonal 2-D filters $\mathbf{C}_x$ and $\mathbf{C}_y$ are simply convolved with each other instead of forming the autocorrelation (1.29). While being a much more efficient approach, splitting suffers from induced anisotropy in the inverse impulse response. Figure 1.26 illustrates this effect in the 2-D plane by comparing the inverse impulse responses of plane-wave filters obtained by spectral factorization and splitting. The splitting response is evidently much less isotropic.

3-D missing data interpolation

Figure 1.27 shows Claerbout's "qdome" synthetic model (Claerbout, 1993, 1999), which models a seismic image of a complicated sedimentary geology. In a data regularization experiment, I randomly remove 60% of the traces in the original model, arriving at the missing data model shown in the right plot of Figure 1.27. The 3-D slope estimates from the input data are shown in the bottom plots of Figure 1.28. The estimates fairly accurately match the slope estimates

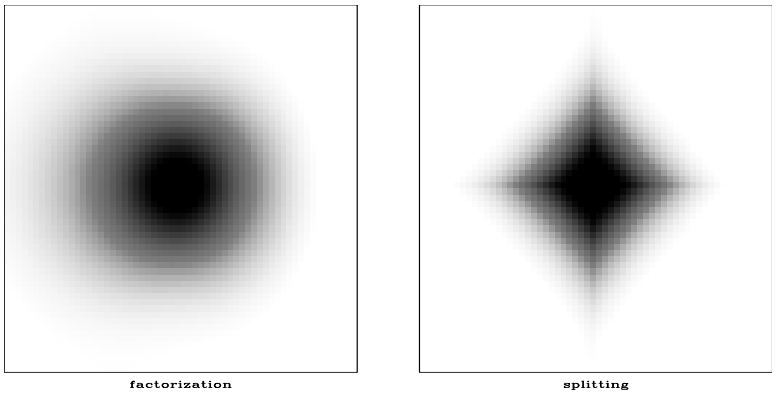

Figure 1.26: Two-dimensional inverse impulse responses for filters constructed with spectral factorization (left) and splitting (right). The splitting response is evidently much less isotropic. regul-bob [ER]

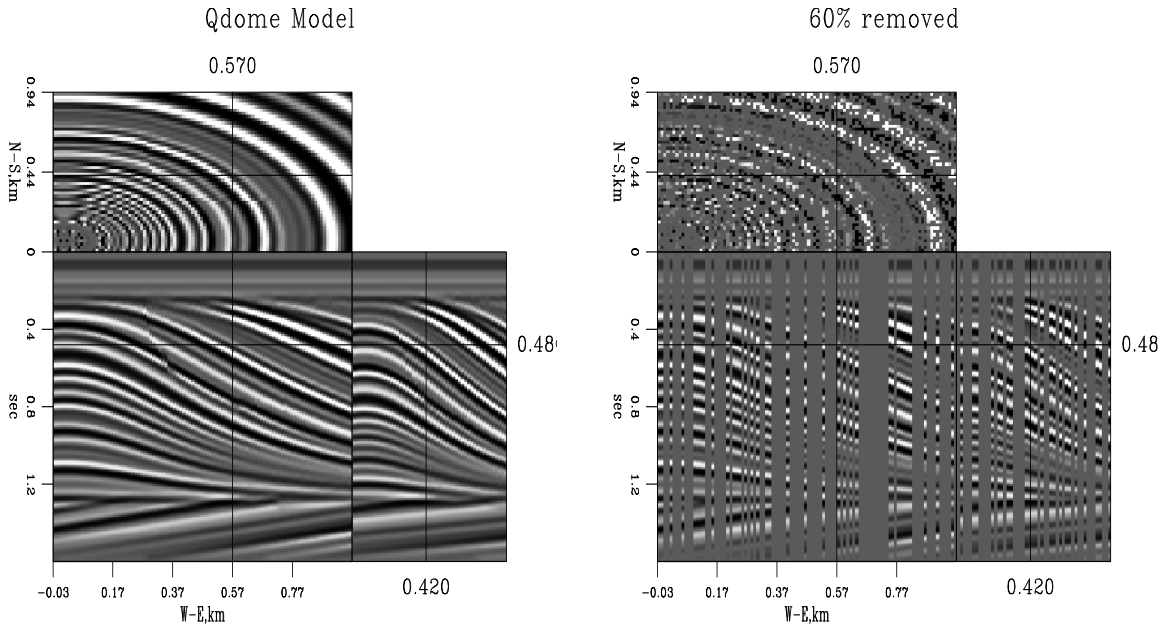

Figure 1.27: Claerbout's "qdome" synthetic model. Left: original model. Right: input to interpolation (60% of the traces removed). regul-qdome [ER]

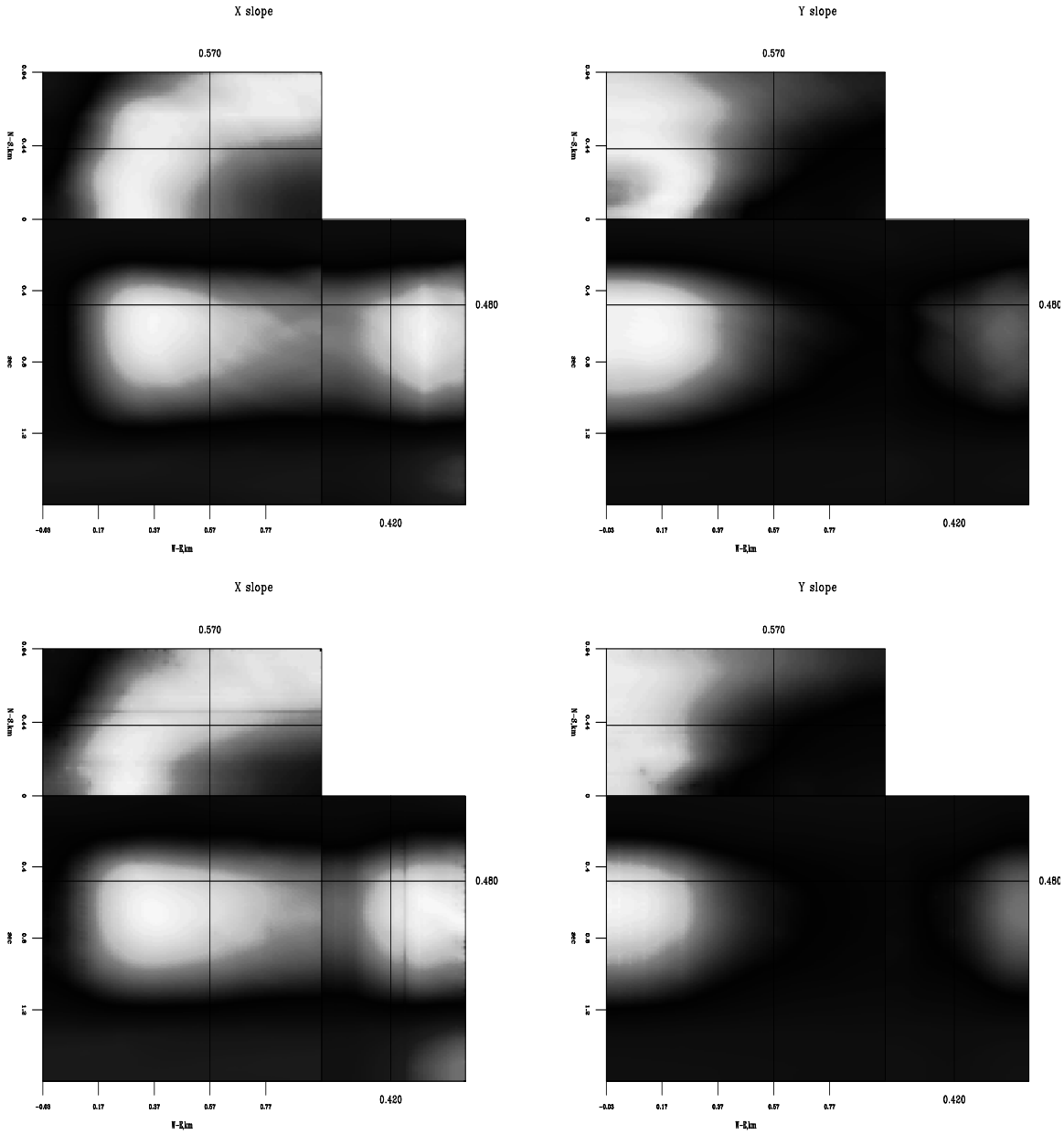

Figure 1.28: Plane-wave slope estimates in the x and y directions (left and right plots, respectively) from the "qdome" model. Top: estimated from the original model. Bottom: estimated from the decimated model. regul-qslope [CR,M]

obtained from the original model (top plots in Figure 1.28). The missing-data interpolation result is shown in Figure 1.29. Most of the original signal has been successfully restored. Some of the fault sharpness is lost in the interpolation result, but all the curved and planar events are accurately preserved. Clapp (2000a) reports a successful interpolation result using a more severe decimation of the same synthetic model. However, he assumes a prior knowledge of the local dip field instead of estimating the dips from the decimated data.

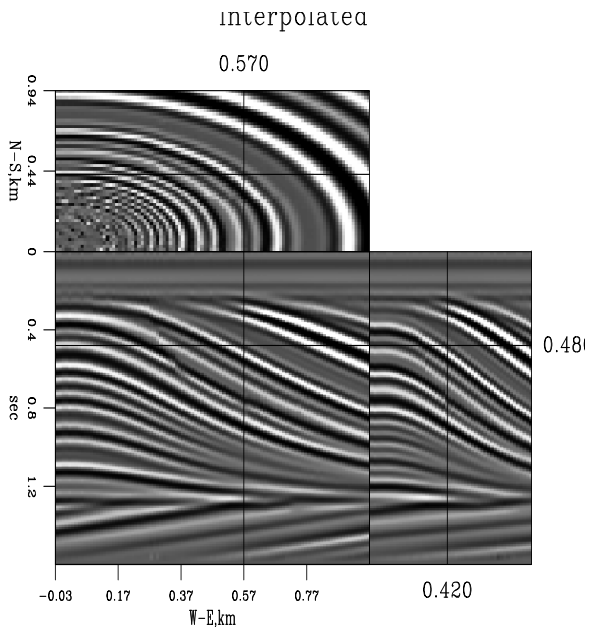

Figure 1.29: Result of missing-data interpolation with a 3-D local plane-wave destruction filter. Compare with Figure 1.27. regul-pmiss [CR]

REGULARIZING REFLECTION SEISMIC DATA WITH OFFSET CONTINUATION

A simple model for reflection seismic data is a set of hyperbolic events on a common midpoint gather. The simplest filter for this model is the first derivative in the offset direction applied after the normal moveout correction.[1] Going one step beyond this simple approximation requires taking the dip moveout (DMO) effect into account (Deregowski, 1986). The DMO effect is fully incorporated in the offset continuation differential equation (Fomel, 1994, 1995a) analyzed theoretically in Chapter 6.

[1] A similar filter appears in velocity estimation with the differential semblance method (Symes and Carazzone, 1991; Symes, 1999).

Offset continuation is a process of seismic data transformation across different offsets (Deregowski and Rocca, 1981; Bolondi et al., 1982; Salvador and Savelli, 1982). As I show in Chapter 6, different types of DMO operators (Hale, 1995) can be regarded as a continuation to zero offset and derived as solutions of an initial-value problem with the revised offset continuation equation (Fomel, 1995b). Within a constant-velocity assumption, this equation not only provides correct traveltimes on the continued sections but also correctly transforms the corresponding wave amplitudes (Fomel, 1995a; Fomel and Bleistein, 1996). Integral offset continuation operators have been derived independently by Stovas and Fomel (1993, 1996), Bagaini and Spagnolini (1996), and Chemingui and Biondi (1994). The 3-D analog is known as azimuth moveout (AMO) (Biondi et al., 1998). In the shot-record domain, integral offset continuation transforms to shot continuation (Schwab, 1993; Bagaini and Spagnolini, 1993; Spagnolini and Opreni, 1996). Integral continuation operators can be applied directly for missing data interpolation and regularization (Bagaini et al., 1994; Mazzucchelli and Rocca, 1999). However, they do not behave well for continuation at small distances in the offset space because of limited integration apertures and, therefore, are not well suited for interpolating neighboring records. Additionally, like all integral (Kirchhoff-type) operators, they suffer from irregularities in the input geometry. The latter problem is addressed by the accurate but expensive method of inversion to common offset (Chemingui, 1999).

In this section, I propose an application of offset continuation in the form of a finite-difference filter for seismic data regularization. The filter is designed in the log-stretch frequency domain, where each frequency slice can be interpolated independently. Small filter size and easy parallelization among different frequencies assure the high efficiency of the proposed approach. Although the offset continuation filter lacks the predictive power of non-stationary prediction-error filters, it is much simpler to handle and serves as a good *a priori* guess of an interpolative filter for seismic reflection data.

I test the proposed method by interpolating randomly missing shot gathers in a constant-velocity synthetic.

Filter design

A particularly efficient implementation of offset continuation results from a log-stretch transform of the time coordinate (Bolondi et al., 1982), followed by a Fourier transform of the stretched time axis. After these transforms, equation (6.1) from Chapter 6 takes the form

$$h\left(\frac{\partial^2 \tilde{P}}{\partial y^2}-\frac{\partial^2 \tilde{P}}{\partial h^2}\right)-i\,\Omega\,\frac{\partial \tilde{P}}{\partial h}=0\,, \tag{1.35}$$

where Ω is the corresponding frequency, h is the half-offset, y is the midpoint, and $\tilde{P}(y,h,\Omega)$ is the transformed data (Fomel, 1995b, 2000). As in other F-X methods, equation (1.35) can be applied independently and in parallel on different frequency slices.

Analogously to the case of the plane-wave-destructor filters discussed in the previous section, we can construct an effective offset-continuation finite-difference filter by studying first the problem of wave extrapolation between neighboring offsets. In the frequency-wavenumber domain, the extrapolation operator is defined in accordance with equation (6.119), as follows:

$$\hat{\hat{P}}(h_2)=\hat{\hat{P}}(h_1)\,Z_\lambda(kh_2)/Z_\lambda(kh_1)\,, \tag{1.36}$$

where $\lambda=(1+i\,\Omega)/2$, and Z_λ is the special function defined in equation (6.120). The wavenumber k corresponds to the midpoint y in the original data domain. In the high-frequency asymptotics, operator (1.36) takes the form

$$\hat{\hat{P}}(h_2)=\hat{\hat{P}}(h_1)\,F(2kh_2/\Omega)/F(2kh_1/\Omega)\exp\left[i\,\Omega\,\psi\,(2kh_2/\Omega-2kh_1/\Omega)\right]\,, \tag{1.37}$$

where functions F and ψ are defined in equations (6.123) and (6.124).

Returning to the original domain, I approximate the continuation operator with a finite-difference filter of the form

$$\hat{P}_{h+1}(Z_y)=\hat{P}_h(Z_y)\frac{G_1(Z_y)}{G_2(Z_y)}\,, \tag{1.38}$$

which is somewhat analogous to (1.15). The coefficients of the filters $G_1(Z_y)$ and $G_2(Z_y)$ are

found by fitting the Taylor series coefficients of the filter response around the zero wavenumber. In the simplest case of 3-point filters[2], this procedure uses four Taylor series coefficients and leads to the following expressions:

$$G_1(Z_y) = 1 - \frac{1 - c_1(\Omega) h_2^2 + c_2(\Omega) h_1^2}{6} + \frac{1 - c_1(\Omega) h_2^2 + c_2(\Omega) h_1^2}{12} \left(Z_y + Z_y^{-1} \right) , \quad (1.39)$$

$$G_2(Z_y) = 1 - \frac{1 - c_1(\Omega) h_1^2 + c_2(\Omega) h_2^2}{6} + \frac{1 - c_1(\Omega) h_1^2 + c_2(\Omega) h_2^2}{12} \left(Z_y + Z_y^{-1} \right) , \quad (1.40)$$

where

$$c_1(\Omega) = \frac{3(\Omega^2 + 9 - 4i\,\Omega)}{\Omega^2 (3 + i\,\Omega)}$$

and

$$c_2(\Omega) = \frac{3(\Omega^2 - 27 - 8i\,\Omega)}{\Omega^2 (3 + i\,\Omega)} .$$

Figure 1.30 compares the phase characteristic of the finite-difference extrapolators (1.38) with the phase characteristics of the exact operator (1.36) and the asymptotic operator (1.37). The match between different phases is poor for very low frequencies (left plot in Figure 1.30) but sufficiently accurate for frequencies in the typical bandwidth of seismic data (right plot in Figure 1.30).

Figure 1.31 compares impulse responses of the inverse DMO operator constructed by the asymptotic $\Omega - k$ operator with those constructed by finite-difference offset continuation. Neglecting subtle phase inaccuracies at large dips, the two images look similar, which indicates the high accuracy of the proposed finite-difference scheme.

When applied on the offset-midpoint plane of an individual frequency slice, the one-dimensional implicit filter (1.38) transforms to a two-dimensional explicit filter with the 2-D

[2] An analogous technique applied to the case of wavefield depth extrapolation with the wave equation would lead to the famous 45-degree implicit finite-difference operator (Claerbout, 1985).

Z-transform

$$G(Z_y, Z_h) = G_1(Z_y) - Z_h G_2(Z_y)\,, \tag{1.41}$$

analogous to filter (1.19) for the case of local plane-wave destruction. Convolution with filter (1.41) is the regularization operator that I propose for regularizing prestack seismic data.

Figure 1.30: Phase of the implicit offset-continuation operators in comparison with the exact solution. The offset increment is assumed to be equal to the midpoint spacing. The left plot corresponds to $\Omega = 1$, the right plot to $\Omega = 10$. regul-arg [CR]

Tests

I start numerical testing of the proposed regularization first on the constant velocity synthetic, where all the assumptions behind the offset continuation equation are valid.

Constant-velocity synthetic

A sinusoidal reflector shown in Figure 1.32 creates complicated reflection data, shown in Figures 1.33 and 1.34. To set up a test for regularization by offset continuation, I removed 90% of randomly selected shot gathers from the input data. The syncline parts of the reflector lead to traveltime triplications at large offsets. A mixture of different dips from the triplications would make it extremely difficult to interpolate the data in individual common-offset gathers,

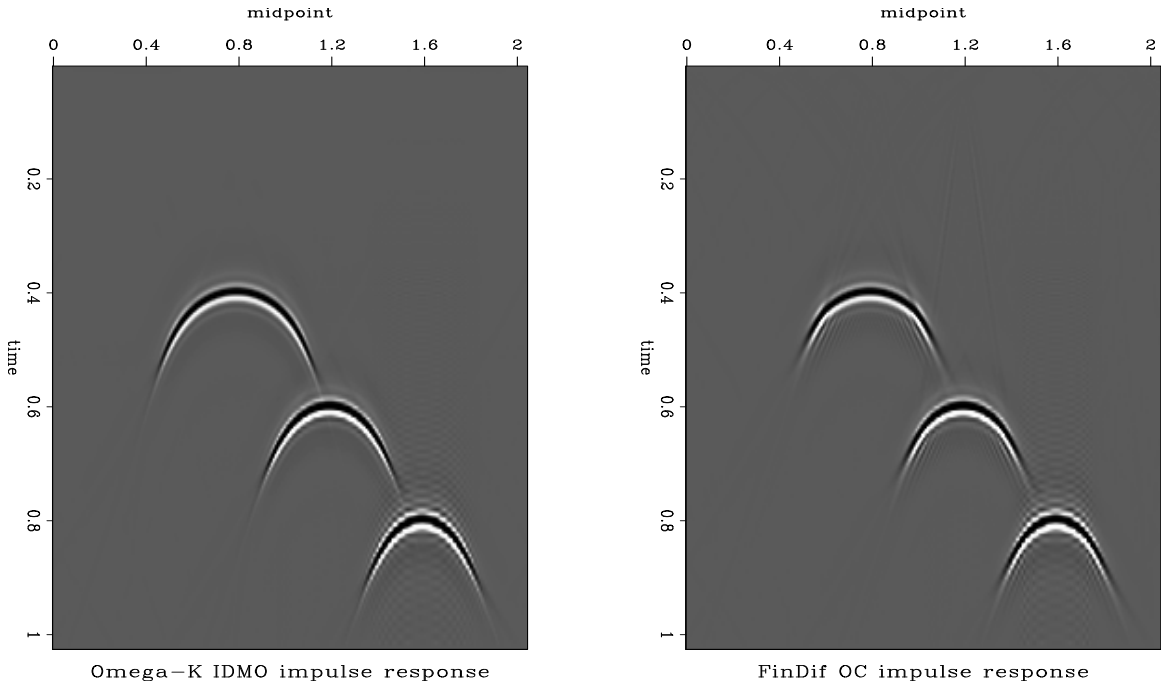

Figure 1.31: Inverse DMO impulse responses computed by the Fourier method (left) and by finite-difference offset continuation (right). The offset is 1 km. regul-off-imp [ER,M]

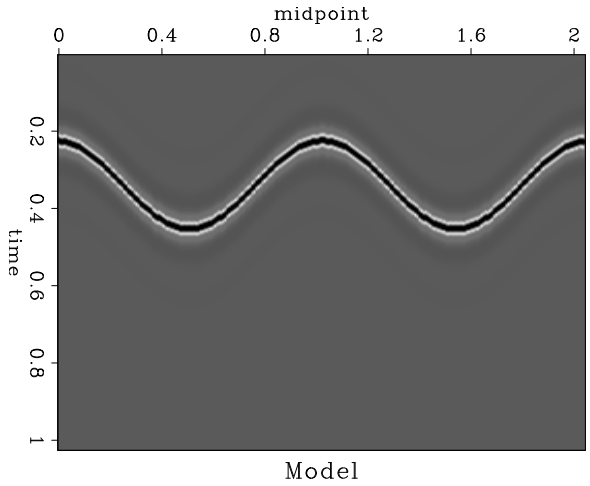

Figure 1.32: Reflector model for the constant-velocity test regul-cup [ER]

such as those shown in Figure 1.33. The plots of time slices after NMO (Figure 1.34) clearly show that the data are also non-stationary in the offset direction. Therefore, a simple offset interpolation scheme is also doomed.

Figure 1.35 shows the reconstruction process on individual frequency slices. Despite the complex and non-stationary character of the reflection events in the frequency domain, the offset continuation equation is able to reconstruct them quite accurately from the decimated data.

Figure 1.36 shows the result of interpolation after the data are transformed back to the time domain. The offset continuation result (right plots in Figure 1.36) reconstructs the ideal data (left plots in Figure 1.33) very accurately even in the complex triplication zones, while the result of simple offset interpolation (left plots in Figure 1.36) fails as expected.

The constant-velocity test results allow us to conclude that, when all the assumptions of the offset continuation theory are met, it provides a powerful method of data regularization.

Being encouraged by the synthetic results, I proceed to a three-dimensional real data test.

3-D data regularization with the offset continuation equation

Similarly to the case of 3-D plane-wave destruction, where the regularization operator is constructed from two orthogonal two-dimensional filters, 3-D differential offset continuation amounts to applying two differential filters, operating on the in-line and cross-line projections of the offset and midpoint coordinates. The corresponding system of differential equations has the form

$$\left\{ \begin{array}{rcl} h_1 \left(\dfrac{\partial^2 \tilde{P}}{\partial y_1^2} - \dfrac{\partial^2 \tilde{P}}{\partial h_1^2} \right) - i\,\Omega \dfrac{\partial \tilde{P}}{\partial h_1} & = & 0\,; \\ h_2 \left(\dfrac{\partial^2 \tilde{P}}{\partial y_2^2} - \dfrac{\partial^2 \tilde{P}}{\partial h_2^2} \right) - i\,\Omega \dfrac{\partial \tilde{P}}{\partial h_2} & = & 0\,, \end{array} \right. \tag{1.42}$$

where y_1 and y_2 correspond to the in-line and cross-line midpoint coordinates, and h_1 and h_2 correspond to the in-line and cross-line offsets. The projection approach is justified in the theory of azimuth moveout (Fomel and Biondi, 1995; Biondi et al., 1998).

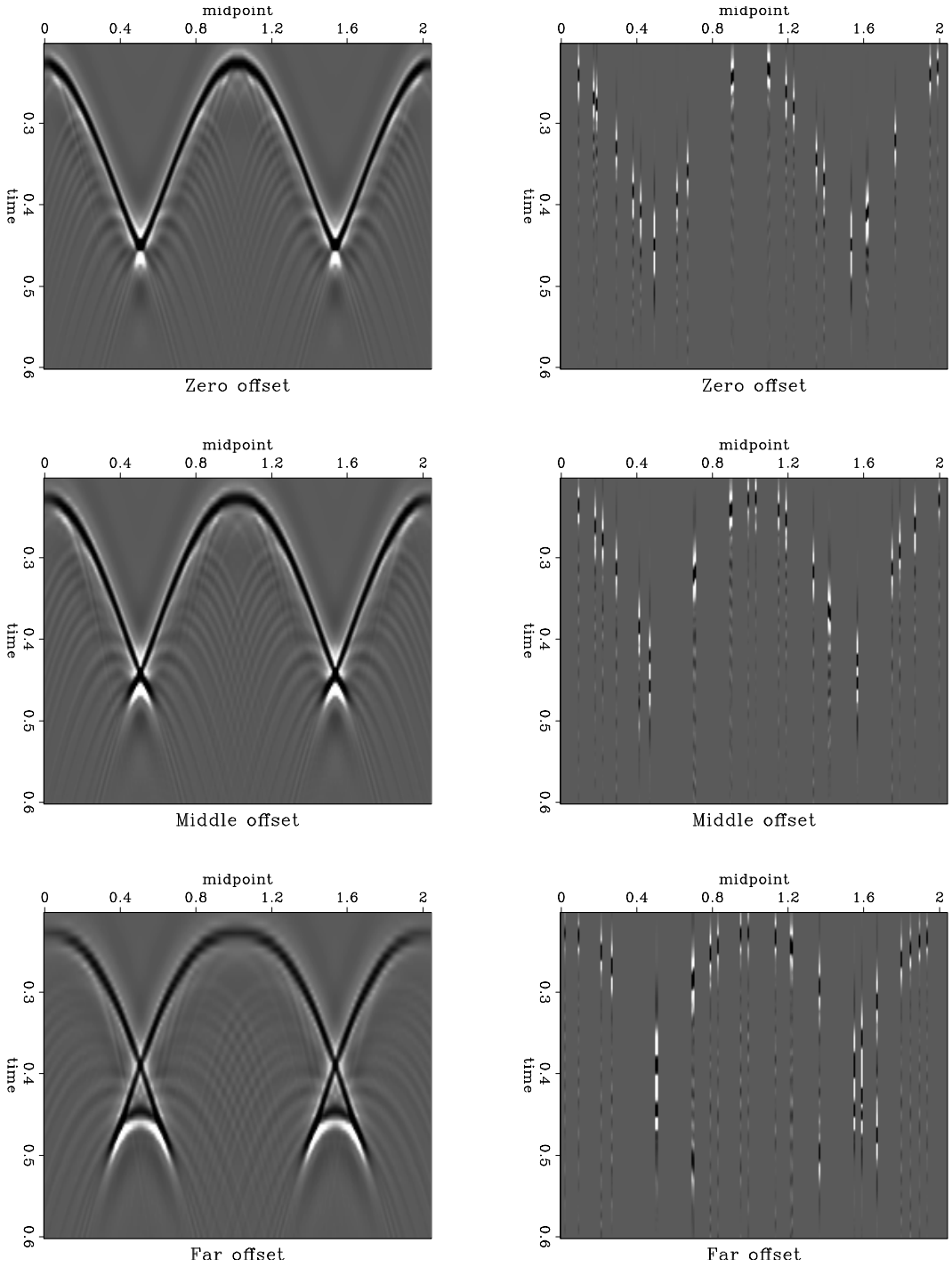

Figure 1.33: Prestack common-offset gathers for the constant-velocity test. Left: ideal data (after NMO). Right: input data (90% of shot gathers removed). Top, center, and bottom plots correspond to different offsets. regul-cupdata [ER,M]

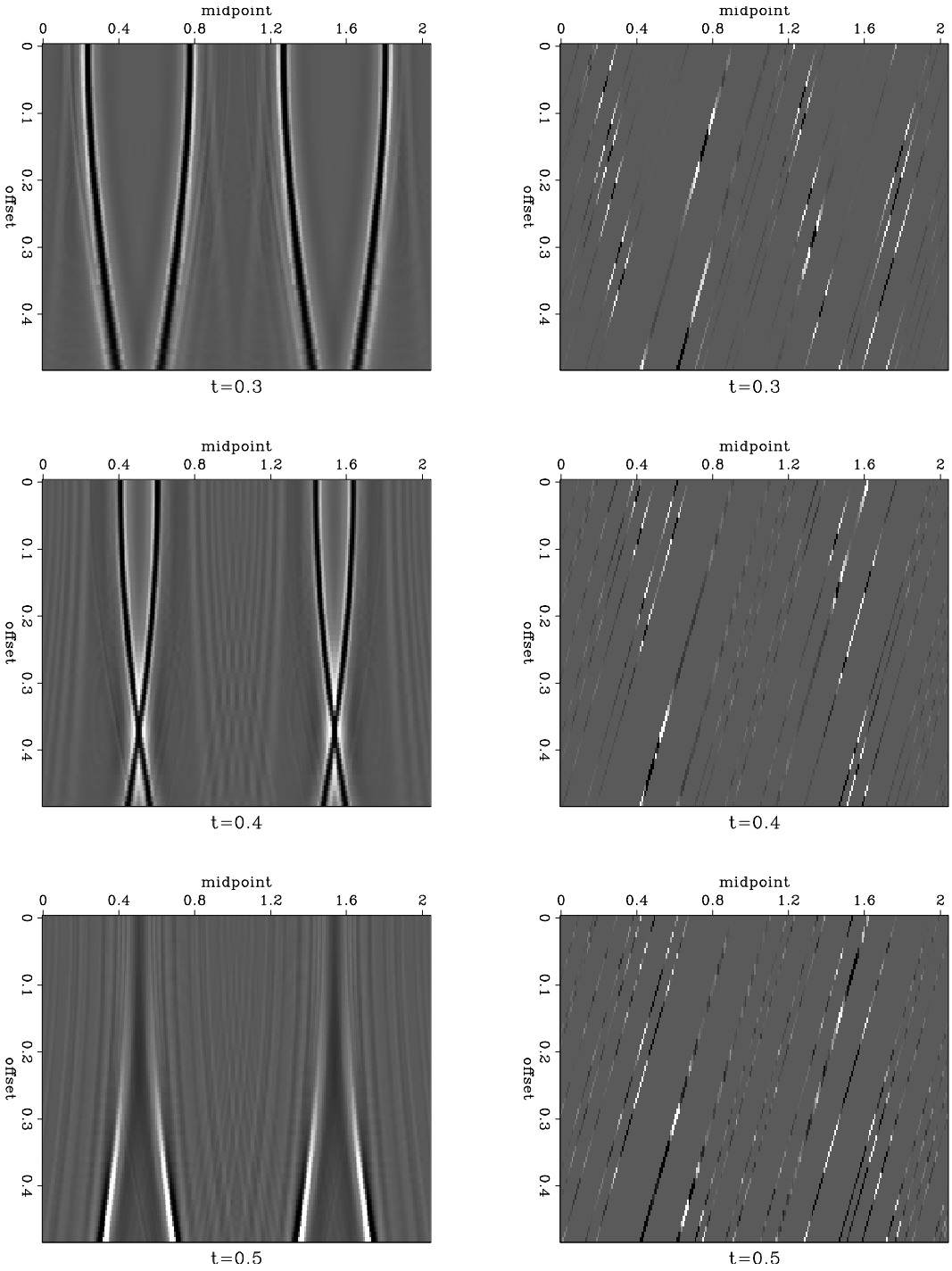

Figure 1.34: Time slices of the prestack data for the constant-velocity test. Left: ideal data (after NMO). Right: input data (90% of random gathers removed). Top, center, and bottom plots correspond to time slices at 0.3, 0.4, and 0.5 s. regul-tslice [ER,M]

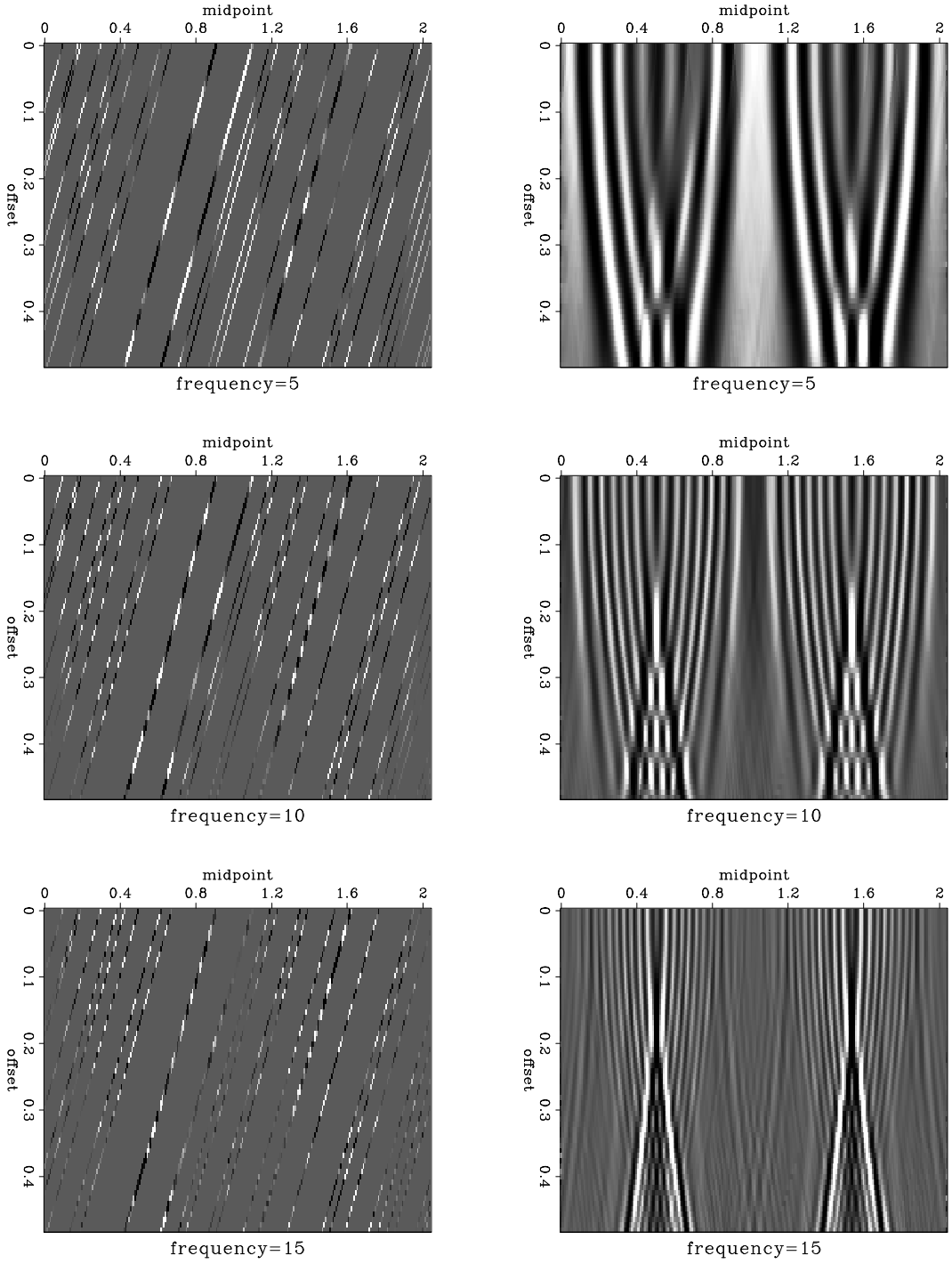

Figure 1.35: Interpolation in frequency slices. Left: input data (90% of the shot gathers removed). Right: interpolation output. Top, bottom, and middle plots correspond to different frequencies. The real parts of the complex-valued data are shown. regul-fslice [ER,M]

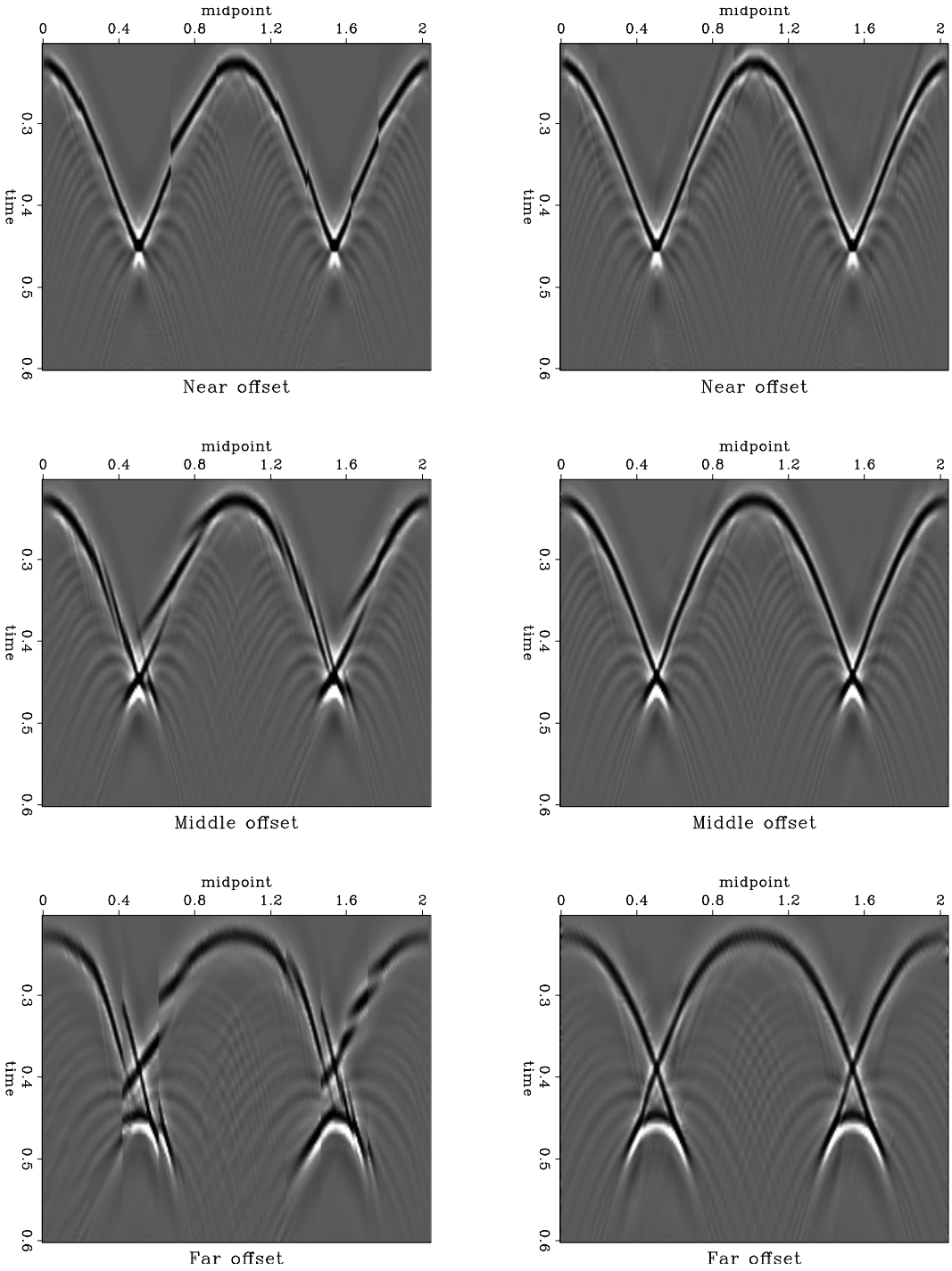

Figure 1.36: Interpolation in common-offset gathers. Left: output of simple offset interpolation. Right: output of offset continuation interpolation. Compare with Figure 1.33. Top, center, and bottom plots correspond to different common-offset gathers. regul-all [ER,M]

The result of a 3-D data regularization test is shown in Figure 1.37. The input data cube corresponds to the one in Figure 1.20. I used neighboring offsets in the in-line and cross-line directions and the differential 3-D offset continuation to reconstruct the empty traces. Although the reconstruction appears less accurate than the plane-wave regularization result of Figure 1.23, it successfully fulfills the following goals:

- The input traces are well hidden in the interpolation result. It is impossible to distinguish between input and interpolated traces.

- The main structural features are restored without using any assumptions about structural continuity in the midpoint domain. Only the physical offset continuity is used.

The lower accuracy of the result in Figure 1.37 in comparison with Figure 1.23 is partially caused by using a simplified missing data interpolation scheme instead of a more accurate regularization approach. It also indicates a possibility of combining offset continuation with midpoint-space plane-wave destruction for achieving an optimal accuracy.

In the next section, I return to the 2-D case to consider an important problem of shot gather interpolation.

Shot continuation

Missing or under-sampled shot records are a common example of data irregularity (Crawley, 2000). The offset continuation approach can be easily modified to work in the shot record domain. With the change of variables $s = y - h$, where s is the shot location, the frequency-domain equation (1.35) transforms to the equation

$$h \left(2 \frac{\partial^2 \tilde{P}}{\partial s \partial h} - \frac{\partial^2 \tilde{P}}{\partial h^2} \right) - i\,\Omega \left(\frac{\partial \tilde{P}}{\partial h} - \frac{\partial \tilde{P}}{\partial s} \right) = 0 \,. \tag{1.43}$$

Unlike equation (1.35), which is second-order in the propagation variable h, equation (1.43) contains only first-order derivatives in s. We can formally write its solution for the initial

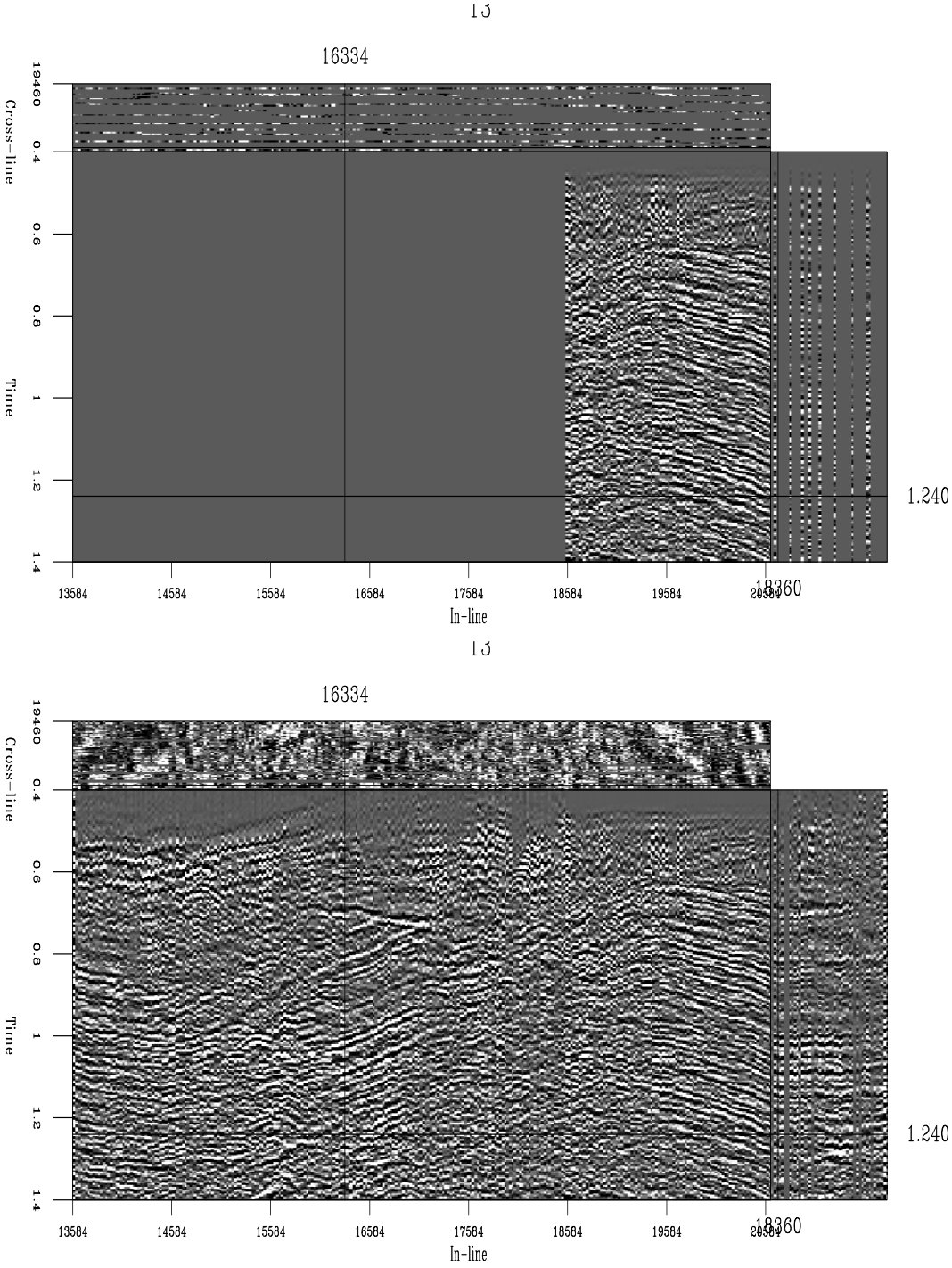

Figure 1.37: 3-D data regularization test. Top: input data, the result of binning in a 50 by 50 meters offset window. Bottom: regularization output. Data from neighboring offset bins in the in-line and cross-line directions were used to reconstruct missing traces. regul-off4 [CR]

conditions at $s = s_1$ in the form of a phase-shift operator:

$$\hat{\hat{P}}(s_2) = \hat{\hat{P}}(s_1) \exp\left[i\, k_h\, (s_2 - s_1)\, \frac{k_h\, h - \Omega}{2 k_h\, h - \Omega} \right], \tag{1.44}$$

where the wavenumber k_h corresponds to the half-offset h. Equation (1.44) is in the mixed offset-wavenumber domain and, therefore, not directly applicable in practice. However, we can use it as an intermediate step in designing a finite-difference shot continuation filter. Analogously to the cases of plane-wave destruction and offset continuation, shot continuation leads us to the rational filter

$$\hat{P}_{s+1}(Z_h) = \hat{P}_s(Z_h) \frac{S(Z_h)}{S(1/Z_h)}\,, \tag{1.45}$$

The filter is non-stationary, because the coefficients of $S(Z_h)$ depend on the half-offset h. We can find them by the Taylor expansion of the phase-shift equation (1.44) around zero wavenumber k_h. For the case of the half-offset sampling equal to the shot sampling, the simplest three-point filter is constructed with three terms of the Taylor expansion. It takes the form

$$S(Z_h) = -\left(\frac{1}{12} + i\, \frac{h}{2\,\Omega} \right) Z_h^{-1} + \left(\frac{2}{3} - i\, \frac{\Omega^2 + 12\,h^2}{12\,\Omega\,h} \right) + \left(\frac{5}{12} + i\, \frac{\Omega^2 + 18\,h^2}{12\,\Omega\,h} \right) Z_h\,. \tag{1.46}$$

Let us consider the problem of doubling the shot density. If we use two neighboring shot records to find the missing record between them, the problem reduces to the least-squares system

$$\begin{bmatrix} \mathbf{S} \\ \bar{\mathbf{S}} \end{bmatrix} \mathbf{p}_s \approx \begin{bmatrix} \bar{\mathbf{S}}\mathbf{p}_{s-1} \\ \mathbf{S}\mathbf{p}_{s+1} \end{bmatrix}, \tag{1.47}$$

where $\mathbf{S}$ denotes convolution with the numerator of equation (1.45), $\bar{\mathbf{S}}$ denotes convolution with the corresponding denominator, $\mathbf{p}_{s-1}$ and $\mathbf{p}_{s+1}$ represent the known shot gathers, and $\mathbf{p}_s$ represents the gather that we want to estimate. The least-squares solution of system (1.47)

takes the form

$$\mathbf{p}_s = \left(\mathbf{S}^T\,\mathbf{S} + \bar{\mathbf{S}}^T\,\bar{\mathbf{S}}\right)^{-1}\left(\mathbf{S}^T\,\bar{\mathbf{S}}\,\mathbf{p}_{s-1} + \bar{\mathbf{S}}^T\,\mathbf{S}\,\mathbf{p}_{s+1}\right)\ . \tag{1.48}$$

If we choose the three-point filter (1.46) to construct the operators $\mathbf{S}$ and $\bar{\mathbf{S}}$, then the inverted matrix in equation (1.48) will have five non-zero diagonals. It can be efficiently inverted with a direct banded matrix solver using the LDL^T decomposition (Golub and Van Loan, 1996). Since the matrix does not depend on the shot location, we can perform the decomposition once for every frequency so that only a triangular matrix inversion will be needed for interpolating each new shot. This leads to an extremely efficient algorithm for interpolating intermediate shot records.

Sometimes, two neighboring shot gathers do not fully constrain the intermediate shot. In order to add an additional constraint, I include a regularization term in equation (1.48), as follows:

$$\mathbf{p}_s = \left(\mathbf{S}^T\,\mathbf{S} + \bar{\mathbf{S}}^T\,\bar{\mathbf{S}} + \epsilon^2\,\mathbf{A}^T\mathbf{A}\right)^{-1}\left(\mathbf{S}^T\,\bar{\mathbf{S}}\,\mathbf{p}_{s-1} + \bar{\mathbf{S}}^T\,\mathbf{S}\,\mathbf{p}_{s+1}\right)\ , \tag{1.49}$$

where $\mathbf{A}$ represents convolution with a three-point prediction-error filter (PEF), and ϵ is a scaling coefficient. The appropriate PEF can be estimated from $\mathbf{p}_{s-1}$ and $\mathbf{p}_{s+1}$ using Burg's algorithm (Burg, 1972, 1975; Claerbout, 1976). A three-point filter leads does not break the five-diagonal structure of the inverted matrix. The PEF regularization attempts to preserve offset dip spectrum in the under-constrained parts of the estimated shot gather.

Figure 1.39 shows the result of a shot interpolation experiment using the constant-velocity synthetic from Figure 1.33. In this experiment, I removed one of the shot gathers from the original data and interpolated it back using equation (1.49). Subtracting the true shot gather from the reconstructed one shows a very insignificant error, which is further reduced by using the PEF regularization (right plots in Figure 1.39). The two neighboring shot gathers used in this experiment are shown in the top plots of Figure 1.38. For comparison, the bottom plots in Figure 1.38 show the simple average of the two shot gathers and its corresponding prediction error. As expected, the error is significantly larger than the error of the shot continuation. An interpolation scheme based on local dips in the shot direction would probably achieve a better

result, but it is generally much more expensive than the shot continuation scheme introduced above.

A similar experiment with real data from a North Sea marine dataset is reported in Figure 1.41. I removed and reconstructed a shot gather from the two neighboring gathers shown in Figure 1.40. The lower parts of the gathers are complicated by salt dome reflections and diffractions with conflicting dips. The simple average of the two input shot gathers (bottom plots in Figure 1.41) works reasonably well for nearly flat reflection events but fails to predict the position of the back-scattered diffractions events. The shot continuation method works well for both types of events (top plots in Figure 1.41). There is some small and random residual error, possibly caused by local amplitude variations.

CONCLUSIONS

Several choices exist in selecting the regularization operator for iterative data regularization.

Splines in tension represent an approach to data regularization suitable for smooth data. The constraint is embedded in a user-specified[3] tension parameter. The two boundary values of tension correspond to cubic and linear interpolation. By applying the method of spectral factorization on a helix, I have been able to define a family of two-dimensional minimum-phase filters, which correspond to the spline interpolation problem with different values of tension. These filters contribute to the collection of useful helical filters. I have used them for preconditioning in data-regularization problems with smooth surfaces. In general, they are applicable for preconditioning various estimation problems with smooth models.

I demonstrate that adaptive local plane-wave destructors with an improved finite-difference design can be a valuable tool in processing multidimensional seismic data. In several examples, I have shown a good performance of plane-wave destructors in application to data regularization. It may be useful to summarize here the similarities and differences between plane-wave destructors and T-X prediction-error filters.

[3]Developing a method for automatic estimation of the appropriate tension parameter from the input data is a challenging open problem. It goes beyond the scope of this work.

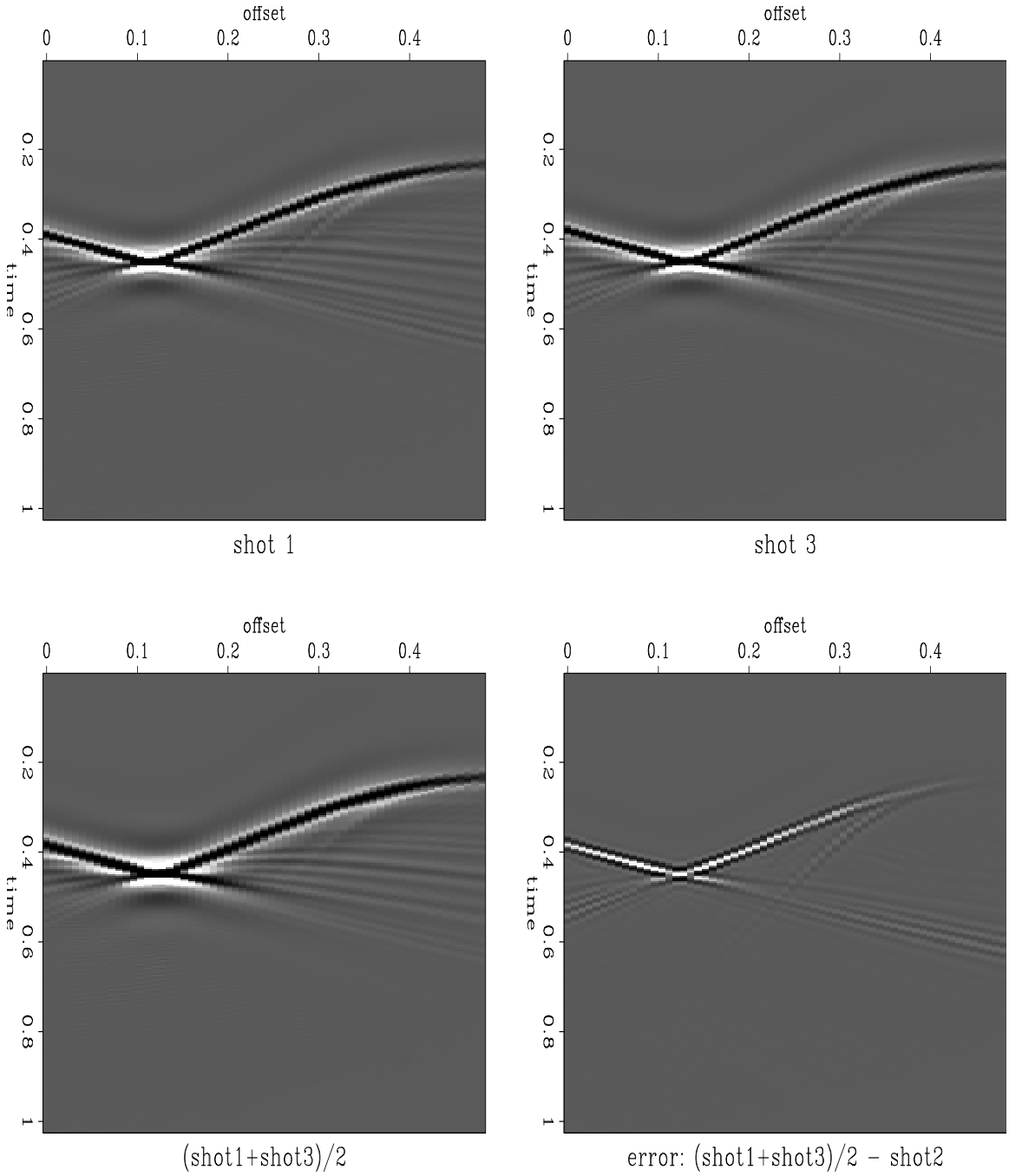

Figure 1.38: Top: Two synthetic shot gathers used for the shot interpolation experiment. An NMO correction has been applied. Bottom: simple average of the two shot gathers (left) and its prediction error (right). regul-shot3 [ER,M]

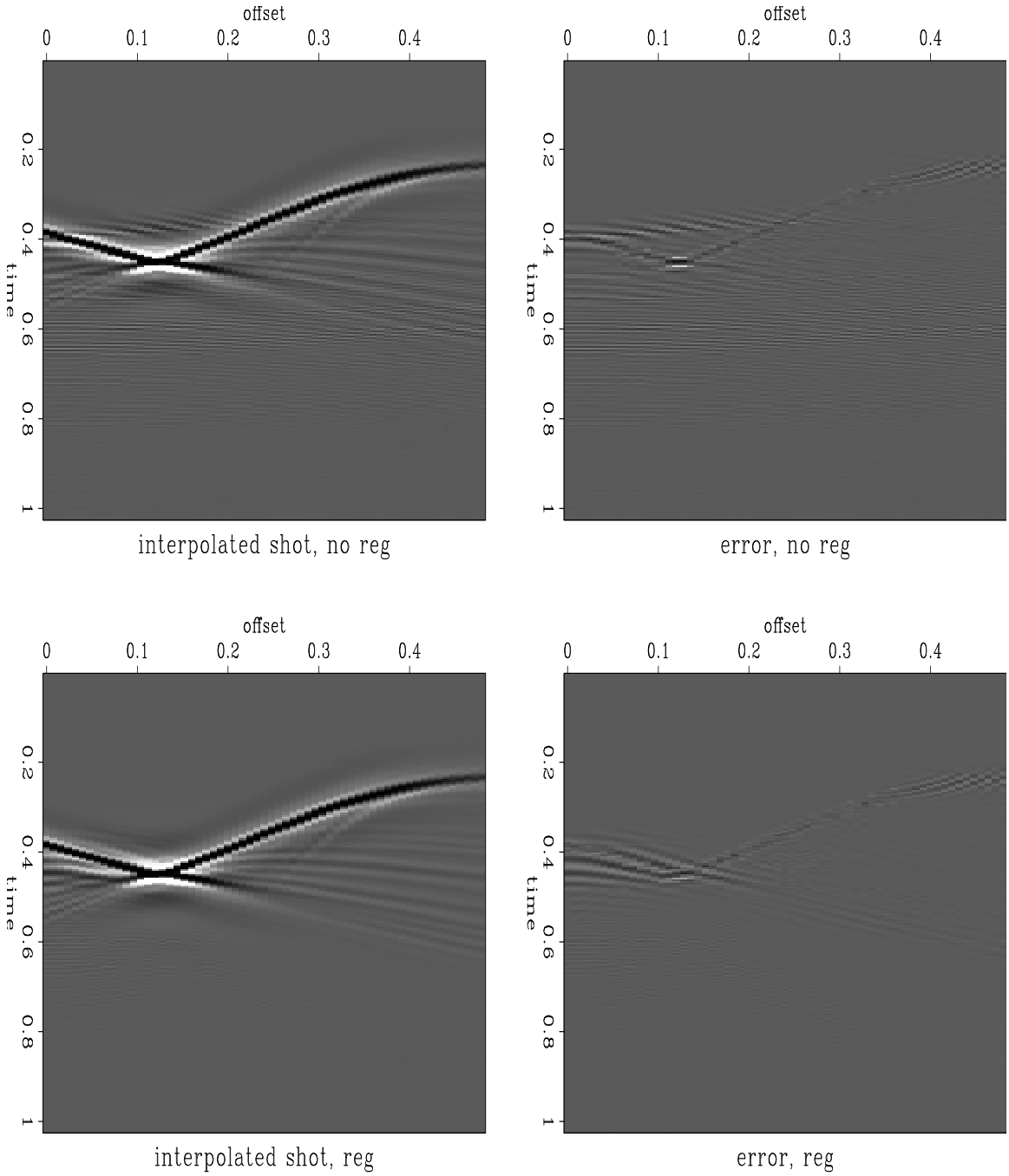

Figure 1.39: Synthetic shot interpolation results. Left: interpolated shot gathers. Right: prediction errors (the differences between interpolated and true shot gathers), plotted on the same scale. Top: without regularization. Bottom: with PEF regularization. regul-shotin [ER]

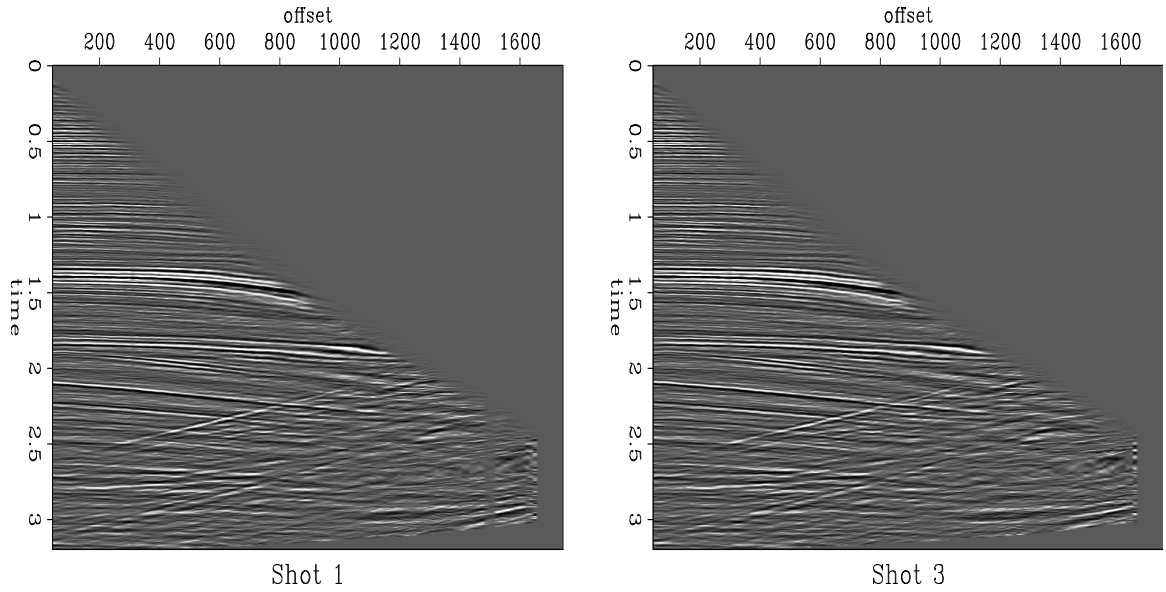

Figure 1.40: Two real marine shot gathers used for the shot interpolation experiment. An NMO correction has been applied. regul-elfshot3 [ER,M]

Similarities:

- Both types of filters operate in the original time-and-space domain of recorded data.
- Both filters aim to predict local plane-wave events in the data.
- In most problems, one filter type can be replaced by the other, and certain techniques, such as Claerbout's trace interpolation method, are common for both approaches.

Differences:

- The design of plane-wave destructors is purely deterministic and follows the plane-wave differential equation. The design of T-X PEF has statistical roots in the framework of the maximum-entropy spectral analysis (Burg, 1975). In principle, T-X PEF can characterize more complex signals than local plane waves.
- In the case of PEF, we estimate filter coefficients. In the case of plane-wave destructors, the estimated quantity is the local plane slope. Several important distinctions follow

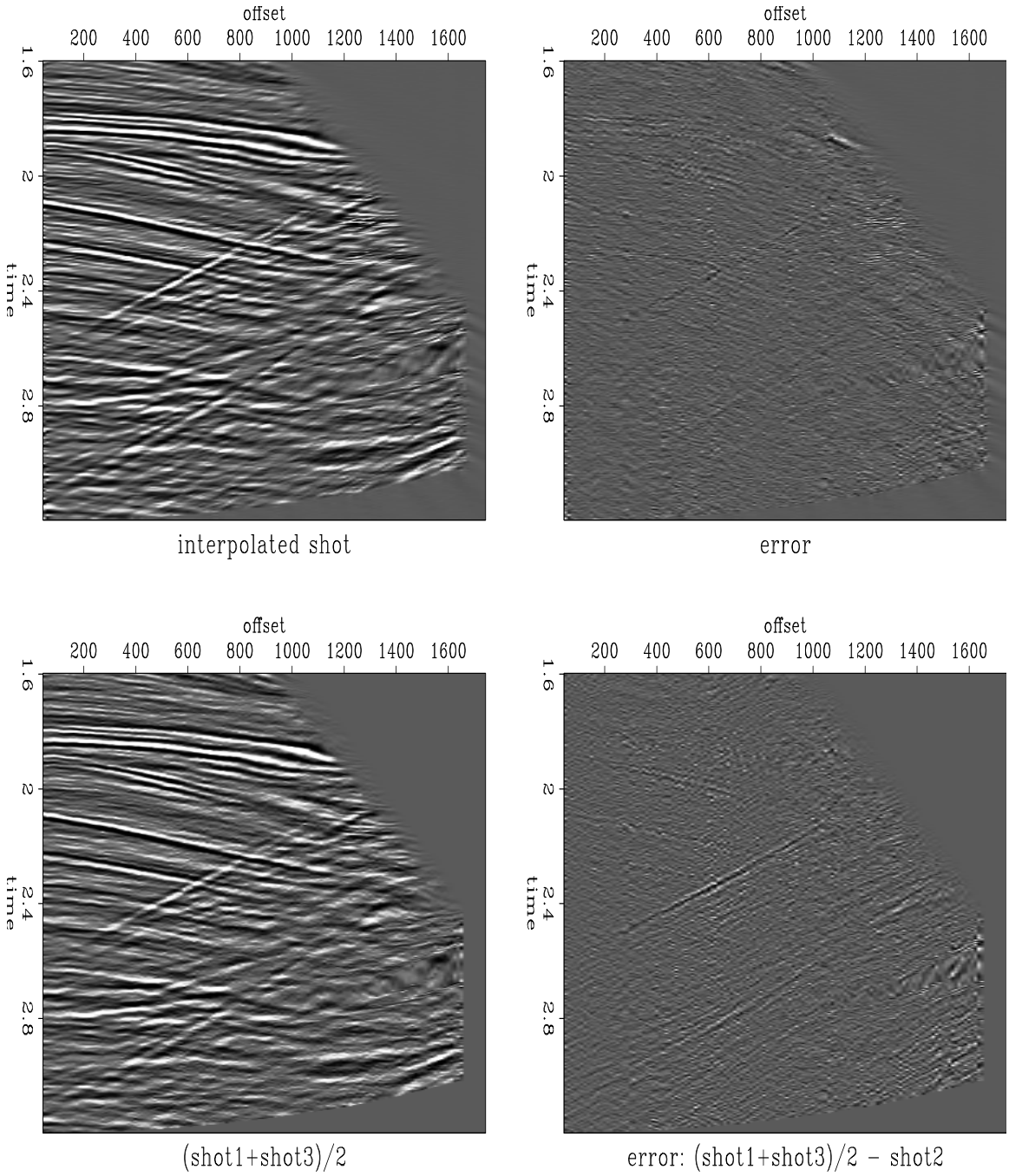

Figure 1.41: Real-data shot interpolation results. Top: interpolated shot gather (left) and its prediction error (right). Bottom: simple average of the two input shot gathers (left) and its prediction error (right). regul-elfshotin [ER]

from that difference:

  - The filter-estimation problem is linear. The-slope estimation problem, in the case of the improved filter design, is non-linear, but allows for an iterative linearization. In general, non-linearity is an undesirable feature because of local minima and the dependence on initial conditions. However, we can sometimes use it creatively. For example, it helped me avoid aliased dips in the trace interpolation example.
  - Non-stationarity is handled gracefully in the local slope estimation. It is a much more difficult issue for PEFs because of the largely under-determined problem.
  - Local slope has a clearly interpretable physical meaning, which allows for easy quality control of the results. The coefficients of T-X PEFs are much more difficult to interpret.

- The efficiency of the two approaches is difficult to compare. Plane-wave destructors are generally more efficient to apply because of the optimally small number of filter coefficients. However, they may require more computation at the estimation stage because of the already mentioned non-linearity problem.

I have shown that a 3-D plane-wave destruction filter can be designed from a pair of two-dimensional filters by using helix transform and the Wilson-Burg spectral factorization algorithm. A special approach to designing plane-wave destructor filters follows from the general B-spline regularization method.

Differential offset continuation provides a valuable tool for regularization of reflection seismic data. Starting from analytical frequency-domain solutions of the offset continuation differential equation, I have designed accurate finite-difference filters for implementing offset continuation as a local convolutional operator. A similar technique works for shot continuation across different shot gathers.

Differential offset continuation serves as a bridge between integral and convolutional approaches to data interpolation. It shares the theoretical grounds with the integral approach but is applied in a manner similar to that of prediction-error filters in the convolutional approach.

Tests with synthetic and real data demonstrate that the offset-continuation regularization can succeed in complex structural situations where more simplistic methods fail.

ACKNOWLEDGMENTS

I thank Jim Berryman for explaining to me the variational derivation of the biharmonic and tension-spline equations.

The 3-D North Sea dataset was released to SEP by Conoco and its partners, BP and Mobil. For the shot continuation test, I used another North Sea dataset, released to SEP by Elf Aquitaine.

Bibliography

Babich, V. M., 1991, Short-wavelength diffraction theory: asymptotic methods: Springer-Verlag, Berlin; New York.

Bagaini, C., and Spagnolini, U., 1993, Common shot velocity analysis by shot continuation operator: 63rd Annual Internat. Mtg., Soc. Expl. Geophys., Expanded Abstracts, 673–676.

Bagaini, C., and Spagnolini, U., 1996, 2-D continuation operators and their applications: Geophysics, **61**, no. 06, 1846–1858.

Bagaini, C., Spagnolini, U., and Pazienza, V. P., 1994, Velocity analysis and missing offset restoration by prestack continuation operators: 64th Annual Internat. Mtg., Soc. Expl. Geophys., Expanded Abstracts, 1549–1552.

Bale, R., and Jakubowicz, H., 1987, Post-stack prestack migration: 57th Annual Internat. Mtg., Soc. Expl. Geophys., Expanded Abstracts, Session:S14.1.

Ben-Avraham, Z., Amit, G., Golan, A., and Begin, Z. B., 1990, The bathymetry of Lake Kinneret and its structural significance: Israel Journal of Earth Sciences, **39**, 77–84.

Beylkin, G., 1985, Imaging of discontinuities in the inverse scattering problem by inversion of a causal generalized Radon transform: Journal of Mathematical Physics, **26**, 99–108.

Biondi, B., and Chemingui, N., 1994a, Transformation of 3-D prestack data by Azimuth Moveout: SEP–**80**, 125–143.

Biondi, B., and Chemingui, N., 1994b, Transformation of 3-D prestack data by azimuth moveout (AMO): 64th Ann. Internat. Mtg., Soc. Expl. Geophys., Expanded Abstracts, 1541–1544.

Biondi, B., and Palacharla, G., 1996, 3-D prestack migration of common-azimuth data: Geophysics, **61**, no. 6, 1822–1832.

Biondi, B., Fomel, S., and Chemingui, N., 1998, Azimuth moveout for 3-D prestack imaging: Geophysics, **63**, no. 02, 574–588.

Biondi, B., 1996, Common-azimuth prestack depth migration of a North Sea data set: SEP–**93**, 1–14.

Black, J. L., Schleicher, K. L., and Zhang, L., 1993, True-amplitude imaging and dip moveout: Geophysics, **58**, no. 1, 47–66.

Bleistein, N., and Cohen, J. K., 1995, The effect of curvature on true amplitude DMO: Proof of concept: ACTI, 4731U0015-2F; CWP-193, Colorado School of Mines.

Bleistein, N., 1984, Mathematical methods for wave phenomena: Academic Press Inc. (Harcourt Brace Jovanovich Publishers), New York.

Bleistein, N., 1990, Born DMO revisited: 60th Annual Internat. Mtg., Soc. Expl. Geophys., Expanded Abstracts, 1366–1369.

Bolondi, G., Loinger, E., and Rocca, F., 1982, Offset continuation of seismic sections: Geophys. Prosp., **30**, no. 6, 813–828.

Briggs, I. C., 1974, Machine contouring using minimum curvature: Geophysics, **39**, no. 1, 39–48.

Brown, M., Clapp, R. G., and Marfurt, K., 1999, Predictive signal/noise separation of groundroll-contaminated data: SEP–**102**, 111–128.

Burg, J. P., 1972, The relationship between maximum entropy spectra and maximum likelihood spectra (short note): Geophysics, **37**, no. 2, 375–376.

Burg, J. P., 1975, Maximum entropy spectral analysis: Ph.D. thesis, Stanford University.

Canales, L. L., 1984, Random noise reduction: 54th Annual Internat. Mtg., Soc. Expl. Geophys., Expanded Abstracts, Session:S10.1.

Canning, A., and Gardner, G. H. F., 1996, Regularizing 3-D data sets with DMO: Geophysics, **61**, no. 04, 1103–1114.

Chemingui, N., and Biondi, B., 1994, Coherent partial stacking by offset continuation of 2-D prestack data: SEP–**82**, 117–126.

Chemingui, N., and Biondi, B., 1996, Handling the irregular geometry in wide azimuth surveys: 66th Annual Internat. Mtg., Soc. Expl. Geophys., Expanded Abstracts, 32–35.

Chemingui, N., 1999, Imaging irregularly sampled 3D prestacked data: Ph.D. thesis, Stanford University.

Claerbout, J. F., 1976, Fundamentals of geophysical data processing: Blackwell.

Claerbout, J. F., 1985, Imaging the Earth's Interior: Blackwell Scientific Publications.

Claerbout, J. F., 1992, Earth Soundings Analysis: Processing Versus Inversion: Blackwell Scientific Publications.

Claerbout, J. F., 1993, 3-D local monoplane annihilator: SEP–**77**, 19–25.

Claerbout, J., 1998a, Multidimensional recursive filters via a helix: Geophysics, **63**, no. 5, 1532–1541.

Claerbout, J., 1998b, Multidimensional recursive filters via a helix: SEP–**97**, 319–335.

Claerbout, J., 1999, Geophysical estimation by example: Environmental soundings image enhancement: Stanford Exploration Project, http://sepwww.stanford.edu/sep/prof/.

Clapp, R. G., and Biondi, B. L., 1998, Regularizing time tomography with steering filters: SEP–**97**, 137–146.

Clapp, R. G., and Biondi, B. L., 2000, Tau tomography with steering filters: 2-D field data example: SEP–**103**, 1–19.

Clapp, R. G., and Brown, M., 2000, $(t - x)$ domain, pattern-based multiple separation: SEP–**103**, 201–210.

Clapp, R. G., Fomel, S., and Claerbout, J., 1997, Solution steering with space-variant filters: SEP–**95**, 27–42.

Clapp, R., Biondi, B., Fomel, S., and Claerbout, J., 1998, Regularizing velocity estimation using geologic dip information: 68th Ann. Internat. Meeting, Soc. Expl. Geophys., Expanded Abstracts, 1851–1854.

Clapp, R. G., Fomel, S., Crawley, S., and Claerbout, J. F., 1999, Directional smoothing of non-stationary filters: SEP–**100**, 197–209.

Clapp, R., 2000a, 3-D steering filters: SEP–**105**, 109–116.

Clapp, R., 2000b, Multiple realizations using standard inversion techniques: SEP–**105**, 67–78.

Cole, S. P., 1995, Passive seismic and drill-bit experiments using 2-D arrays: Ph.D. thesis, Stanford University.

Courant, R., 1962, Methods of mathematical physics: Interscience Publishers, New York.

Crawley, S., Clapp, R., and Claerbout, J., 1998, Decon and interpolation with nonstationary filters: SEP–**97**, 183–192.

Crawley, S., Clapp, R., and Claerbout, J., 1999, Interpolation with smoothly nonstationary prediction-error filters: 69th Ann. Internat. Meeting, Soc. Expl. Geophys., Expanded Abstracts, 1154–1157.

Crawley, S., 1999, Interpolation with smoothly nonstationary prediction-error filters: SEP–**100**, 181–196.

Crawley, S., 2000, Seismic trace interpolation with nonstationary prediction-error filters: Ph.D. thesis, Stanford University.

de Boor, C., 1978, A practical guide to splines: Springer-Verlag.

Deregowski, S. M., and Rocca, F., 1981, Geometrical optics and wave theory of constant offset sections in layered media: Geophys. Prosp., **29**, no. 3, 374–406.

Deregowski, S. M., 1986, What is DMO: First Break, **4**, no. 7, 7–24.

Fomel, S., and Biondi, B., 1995, The time and space formulation of azimuth moveout: 65th Ann. Internat. Mtg., Soc. Expl. Geophys., Expanded Abstracts, 1449–1452.

Fomel, S., and Bleistein, N., 1996, Amplitude preservation for offset continuation: Confirmation for Kirchhoff data: SEP–**92**, 219–227.

Fomel, S., and Claerbout, J., 1995, Searching the Sea of Galilee: The splendors and miseries of iteratively reweighted least squares: SEP–**84**, 259–270.

Fomel, S., Bleistein, N., Jaramillo, H., and Cohen, J. K., 1996, True amplitude DMO, offset continuation and AVA/AVO for curved reflectors: 66th Annual Internat. Mtg., Soc. Expl. Geophys., Expanded Abstracts, 1731–1734.

Fomel, S. B., 1994, Kinematically equivalent differential operator for offset continuation of seismic sections: Russian Geology and Geophysics, **35**, no. 9, 122–134.

Fomel, S., 1995a, Amplitude preserving offset continuation in theory Part 1: The offset continuation equation: SEP–**84**, 179–198.

Fomel, S., 1995b, Amplitude preserving offset continuation in theory Part 2: Solving the equation: SEP–**89**, 109–132.

Fomel, S., 1996, Stacking operators: Adjoint versus asymptotic inverse: SEP–**92**, 267–292.

Fomel, S., 2000, Seismic data interpolation with the offset continuation equation: SEP–**103**, 237–254.

Fung, Y. C., 1965, Foundations of solid mechanics: Prentice-Hall.

Gazdag, J., 1978, Wave equation migration with the phase shift method: Geophysics, **43**, 1342–1351.

Goldin, S. V., and Fomel, S. B., 1995, Estimation of reflection coefficient in DMO: Russian Geology and Geophysics, **36**, no. 4, 103–115.

Goldin, S. V., 1988, Transformation and recovery of discontinuities in problems of tomographic type: Institute of Geology and Geophysics, Novosibirsk (in Russian).

Goldin, S., 1990, A geometric approach to seismic processing: the method of discontinuities: SEP–**67**, 171–210.

Goldin, S. V., 1994, Superposition and continuation of tranformations used in seismic migration: Russian Geology and Geophysics, **35**, no. 9, 131–145.

Golub, G. H., and Van Loan, C. F., 1996, Matrix computations: The John Hopkins University Press.

Gradshtein, I. S., and Ryzhik, I. M., 1994, Table of integrals, series, and products: Boston: Academic Press.

Haddon, R. A. W., and Buchen, P. W., 1981, Use of Kirchhoff's formula for body wave calculations in the earth: Geophys. J. Roy. Astr. Soc., **67**, 587–598.

Hale, I. D., 1983, Dip moveout by Fourier transform: Ph.D. thesis, Stanford University.

Hale, D., 1984, Dip-moveout by Fourier transform: Geophysics, **49**, no. 6, 741–757.

Hale, D., 1991, Course notes: Dip moveout processing: Soc. Expl. Geophys.

Hale, D., Ed. **DMO processing**. Society Of Exploration Geophysicists, 1995.

Liner, C. L., and Cohen, J. K., 1988, An amplitude-preserving inverse of Hale's DMO: 58th Annual Internat. Mtg., Soc. Expl. Geophys., Expanded Abstracts, 1117–1120.

Liner, C., 1990, General theory and comparative anatomy of dip moveout: Geophysics, **55**, no. 5, 595–607.

Liner, C. L., 1991, Born theory of wave-equation dip moveout: Geophysics, **56**, no. 2, 182–189.

Mazzucchelli, P., and Rocca, F., 1999, Regularizing land acquisitions using shot continuation operators: effects on amplitudes: 69th Annual Internat. Mtg., Soc. Expl. Geophys., Expanded Abstracts, 1995–1998.

Nolet, G., Ed., 1987, Seismic tomography: with applications in global seismology and exploration geophysics D. Reidel.

Notfors, C. D., and Godfrey, R. J., 1987, Dip moveout in the frequency-wavenumber domain (short note): Geophysics, **52**, no. 12, 1718–1721.

Petkovsek, M., Wilf, H. S., and Zeilberger, D., 1996, $A = B$: A K Peters Ltd., Wellesley, MA.

Ronen, S., Sorin, V., and Bale, R., 1991, Spatial dealiasing of 3-D seismic reflection data: Geophysical Journal International, pages 503–511.

Ronen, J., 1987, Wave equation trace interpolation: Geophysics, **52**, no. 7, 973–984.

Ronen, S., 1994, Handling irregular geometry: Equalized DMO and beyond: 64th Ann. Internat. Mtg., Soc. Expl. Geophys., Expanded Abstracts, 1545–1548.

Salvador, L., and Savelli, S., 1982, Offset continuation for seismic stacking: Geophys. Prosp., **30**, no. 6, 829–849.

Sandwell, D. T., 1987, Biharmonic spline interpolation of GEOS-3 and SEASAT altimeter data: Geophys. Res. Letters, **14**, no. 2, 139–142.

Santos, L. T., Schleicher, J., and Tygel, M., 1997, 2.5-D true-amplitude offset continuation: Journal of Seismic Exploration, **6**, no. 2-3, 103–116.

Schwab, M., and Claerbout, J., 1995, The interpolation of a 3-D data set by a pair of 2-D filters: SEP–**84**, 271–278.

Schwab, M., 1993, Shot gather continuation: SEP–**77**, 117–130.

Schwab, M., 1998, Enhancement of discontinuities in seismic 3-D images using a Java estimation library: Ph.D. thesis, Stanford University.

Schweikert, D. G., 1966, An interpolation curve using a spline in tension: Journal of Mathematics and Physics, **45**, 312–313.

Smith, W. H. F., and Wessel, P., 1990, Gridding with continuous curvature splines in tension: Geophysics, **55**, no. 3, 293–305.

Spagnolini, U., and Opreni, S., 1996, 3-D shot continuation operator: 66th Annual Internat. Mtg., Soc. Expl. Geophys., Expanded Abstracts, 439–442.

Spitz, S., 1991, Seismic trace interpolation in the f-x domain: Geophysics, **56**, no. 6, 785–794.

Stolt, R. H., 1978, Migration by Fourier transform: Geophysics, **43**, no. 1, 23–48.

Stovas, A. M., and Fomel, S. B., 1993, Kinematically equivalent DMO operators: Presented at the SEG-Moscow, SEG-Moscow.

Stovas, A. M., and Fomel, S. B., 1996, Kinematically equivalent integral DMO operators: Russian Geology and Geophysics, **37**, no. 2, 102–113.

Swain, C. J., 1976, A FORTRAN IV program for interpolating irregularly spaced data using the difference equations for minimum curvature: Computers and Geosciences, **1**, 231–240.

Symes, W. W., and Carazzone, J. J., 1991, Velocity inversion by differential semblance optimization: Geophysics, **56**, no. 5, 654–663.

Symes, W. W., 1999, All stationary points of differential semblance are asymptotic global minimizers: Layered acoustics: SEP–**100**, 71–92.

Tenenbaum, M., and Pollard, H., 1985, Ordinary differential equations : an elementary textbook for students of mathematics, engineering, and the sciences: Dover Publications.

Timoshenko, S., and Woinowsky-Krieger, S., 1968, Theory of plates and shells: McGraw-Hill.

Červeň, V., Molotkov, I. A., and Pšenčik, I., 1977, Ray method in seismology: Univerzita Karlova, Praha.

Watson, G. N., 1952, A treatise on the theory of Bessel functions: Cambridge University Press, 2nd edition.

Woodward, M. J., Farmer, P., Nichols, D., and Charles, S., 1998, Automated 3-D tomographic velocity analysis of residual moveout in prestack depth migrated common image point gathers: 68th Annual Internat. Mtg., Soc. Expl. Geophys., Expanded Abstracts, 1218–1221.

Zhao, Y., 1999, Helix derivative and low-cut filters' spectral feature and application: SEP–**100**, 235–250.

Zhou, B., Mason, I. M., and Greenhalgh, S. A., 1996, An accurate formulation of log-stretch dip moveout in the frequency-wavenumber domain: Geophysics, **61**, no. 03, 815–820.